International Journal of Plasticity 157 (2022) 103401

Contents lists available at ScienceDirect

International Journal of Plasticity

journal homepage: www.elsevier.com/locate/ijplas

A peridynamic approach to solving general discrete dislocation dynamics problems in plasticity and fracture: Part I. Model description and verification

Wenbo Dong [a], Hengjie Liu [a], Juan Du [b], Xu Zhang [c], Minsheng Huang [a,d,**], Zhenhuan Li [a,d], Ziguang Chen [a,d,*], Florin Bobaru [e]

[a] *Department of Engineering Mechanics, School of Aerospace Engineering, Huazhong University of Science and Technology, Wuhan, 430074, China*
[b] *Science and Technology on Reactor System Design Technology Laboratory, Nuclear Power Institute of China, Chengdu 610213, China*
[c] *School of Mechanics and Aerospace Engineering, Southwest Jiaotong University, Chengdu 610031, China*
[d] *Hubei Key Laboratory of Engineering Structural Analysis and Safety Assessment, 1037 Luoyu Road, Wuhan, 430074, China*
[e] *Department of Mechanical and Materials Engineering, University of Nebraska-Lincoln, Lincoln, NE, 68588-0526, USA*

ARTICLE INFO

Keywords:
Discrete dislocation dynamics
Peridynamics
Plasticity
Damage
Nonlocal
Cracks

ABSTRACT

In this paper, we present a peridynamic (PD)-based solution for discrete dislocation dynamics (DDD) problems using the superposition (SP) framework. By replacing the classical surface traction in the complementary problem with a nonlocal/peridynamic one, the SP DDD-PD scheme can simulate arbitrary domains, including those with pre-damage, cracks, and voids of arbitrary shapes, without explicitly tracking boundaries, interfaces, cracks, etc. The new SP DDD-PD scheme is verified for the boundary value problems (BVPs) for single dislocation, multiple dislocations, dislocation emitted from a crack tip, and dislocation-void interaction. The numerical results are compared with those from other existing schemes: the discrete-continuous (DC) DDD-PD, and the SP DDD-FEM. The new SP DDD-PD is more accurate than the DC DDD-PD scheme, especially near dislocation cores and in problems with dislocations near defects (damage or interfaces). The high accuracy of the new SP DDD-PD near dislocation cores makes it suitable to model dislocation-based plasticity and fracture, problems that are studied in part II of this work.

1. Introduction

Dislocations, common line defects in crystals, are the main carriers of plastic deformation in crystalline materials (Anderson et al., 2017). Discrete dislocation dynamics (DDD) can track the dynamic evolution of discrete dislocations, including dislocation nucleation and annihilation, dislocation motion, and the interaction between dislocations and other defects/obstacles (Chatterjee et al., 2021; Guo et al., 2021), which are fundamental to the prediction of plastic deformation in crystalline materials (Anderson et al., 2017; Du et al., 2022) and the understanding of ductile/brittle transition in environmentally-assisted cracking, such as hydrogen embrittlement (Connolly et al., 2019; Deutges et al., 2015; Liang et al., 2021; Zhao et al., 2018), liquid metal embrittlement (Nam and Srolovitz, 2009) and stress-corrosion cracking (Oger et al., 2020). Compared with molecular dynamics (MD) simulations, DDD can model relatively

---

* Corresponding author.
** Corresponding author.
E-mail addresses: mshuang@hust.edu.cn (M. Huang), zchen@hust.edu.cn (Z. Chen).

https://doi.org/10.1016/j.ijplas.2022.103401
Received 13 May 2022; Received in revised form 13 August 2022;
Available online 15 August 2022

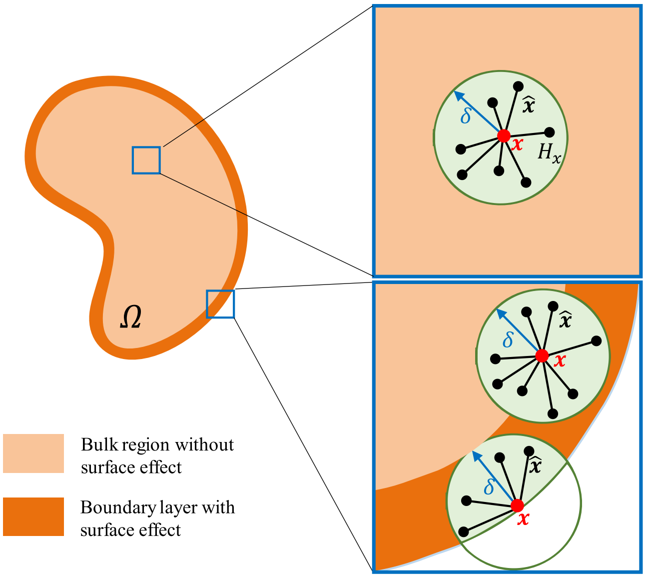

Fig. 1. In the horizon regions H_x delineated by the green circles, the central points x interact directly with any surrounding point $\hat{x}$. Materials points in the bulk have full horizons (full circular areas), while those in the boundary layer (with thickness δ) have partial horizons (partial disks in 2D, or partial spherical volumes in 3D).

larger temporal and spatial scales while correctly accounting for the physical mechanisms present in plastic deformations.

DDD models are usually based on continuum mechanics concepts and lead to having to solve boundary value problems (BVPs) for partial differential equations. DDD frameworks can be classified into two categories: superposition (SP) scheme, and the discrete-continuous (DC) coupling scheme.

The SP scheme was first proposed in Van der Giessen and Needleman (1995). In this scheme, the BVPs are solved by superposing the analytical solutions (stress, strain and displacement) in an infinite solid containing discrete dislocations to numerical solutions in the given finite elastic solid with auxiliary boundary conditions. The finite element method (FEM) (Fivel and Canova, 1999; Liang et al., 2015; Lu et al., 2022) and boundary element method (BEM) (El-Awady et al., 2008; Takahashi and Ghoniem, 2008) have been extensively used for the SP scheme of DDD to simulate the dynamic behavior of dislocations evolution and the plastic deformation of crystalline materials. With the individual dislocation fields for an edge dislocation in a traction-free half-space, the effects of dislocation source and obstacle densities on the crack growth resistance were studied in Cleveringa et al. (2000); Freund (1993). Following (Cleveringa et al., 2000), DDD simulations with the SP scheme have been applied to various ductile fracture problems of crystalline materials at the micro-scale (Cleveringa et al., 2001; Irani et al., 2017; O'day and Curtin, 2005; Van der Giessen et al., 2001).

In all DC schemes, plastic strain or displacement discontinuity induced by the dislocation slip are embedded in the continuum model. The analytical solutions of the dislocation stress fields for the infinite domain are not needed in this case; instead, equilibrium fields are determined directly for the finite domain, by using, for example, the FEM (Cui et al., 2022; Devincre et al., 2011). To more accurately capture the stress and strain fields near the dislocation core, the phase field method (Wang et al., 2001) or the extended finite element method (XFEM) (Huang et al., 2020; Liang et al., 2019; Oswald et al., 2009) have been applied in the DC scheme., The Peach-Koehler force on each dislocation can be directly computed from the finite element stress field, but, for high accuracy, it requires enrichment around the core, based on the analytical solutions. These methods still have difficulties dealing with simulating dislocation-to-crack transitions and dynamic crack growth (Mehrmashhadi et al., 2020).

Motivated by unifying continuum and discontinuum mechanics (fracture mechanics and fragmentation, molecular dynamics, etc.) (Bobaru et al., 2016; Silling, 2000), Silling introduced the theory of peridynamics (PD), a nonlocal alternative to classical continuum mechanics. In the PD theory, spatial derivatives are replaced with an integral term in the equations of motion. Therefore, PD can effectively simulate problems with discontinuities in the deformation field (Silling, 2000; Silling and Askari, 2005) and has been successfully applied in many other areas to solve some great challenges (Chen et al., 2021; Jafarzadeh et al., 2018; Katiyar et al., 2020; Xu et al., 2018). A PD formulation has recently been applied to model mechanical fields induced by dislocations in the DC scheme context (Zhao and Shen, 2021). When dislocations are far from boundaries and from each other, the scheme works well. However, when one considers dislocation kinetics, the dislocations inevitably interact with boundaries or among them, and the DC scheme of DDD in the framework of PD (DDD-PD model) is not applicable.

In this paper, we introduce the SP scheme for a DDD-PD model. Nonlocal interactions in the model are used to replace classical surface tractions (on the complementary problem traction-boundary), which eliminates the need for explicitly tracking boundaries, interfaces, cracks, etc., and makes the model very general, flexible, thus able to naturally handle material damage and fracture processes. Another advantage is that BVPs for plastic deformations in domains with voids, pre-damage/pre-cracks, etc., are no more complicated to solve than those in regular domains. Moreover, no special treatments are needed for dislocation-damage and

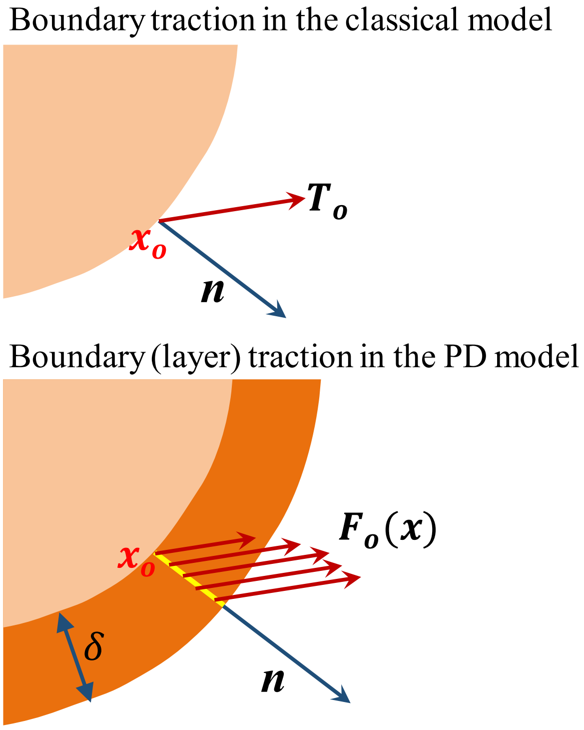

Fig. 2. Boundary traction in the classical model and the corresponding boundary layer traction in the PD model.

dislocation-interface interactions, which are generally complex problems for DDD schemes based on classical models.

The paper is organized as follows: In Section 2, the bond-based peridynamic theory is reviewed briefly; in Section 3, the SP scheme of the DDD-PD model is proposed and described; in Section 4, verification problems for a single dislocation, multiple edge dislocations, dislocation emitted from the crack tip, and edge dislocation-void interaction are shown; Section 5 contains main conclusions.

In Part II of this work (Dong et al., al.), we extend the model to consider the autonomous interactions between dislocations and cracks by including bond-breaking and nucleation, glide, annihilation, and motion of dislocations. The new model can simulate dislocation-based elastoplastic deformation and fracture without a preset cracking path or a cohesive zone model. A smooth and wavy crack path could be obtained for a Mode I elastoplastic fracture, matching well with experimental observations.

2. Brief introduction to bond-based peridynamics

Peridynamics (PD) (Silling, 2000), a nonlocal alternative of the classical continuum mechanics, replaces spatial derivatives by integrals, making it naturally consistent for problems with displacement discontinuities. Without any extra failure criteria beyond a bond-failure law calibrated to Griffiths fracture energy, the natural evolution of arbitrary damage and cracks can be simulated by a PD model. The original bond-based PD was later generalized by the state-based PD (Silling et al., 2007). The bond-based PD has been successfully applied to various problems (Chen and Bobaru, 2015; Cheng et al., 2015; De Meo et al., 2016; Jafarzadeh et al., 2019; Wu et al., 2021). In this work, our focus is on introducing a nonlocal PD platform for DDD. The limitation of bond-based PD to simulating materials with a fixed Poisson's ratio is easily remove by using state-based PD (Zhao and Shen, 2021).

In PD, each material point interacts nonlocally with its surrounding points within a finite distance, as shown in Fig. 1. The equations of motion for the bond-based PD are given as:

$$\rho(\boldsymbol{x})\ddot{\boldsymbol{u}}(\boldsymbol{x},t) = \int_{H_x} \boldsymbol{f}(\boldsymbol{u}(\boldsymbol{x},t)-\boldsymbol{u}(\widehat{\boldsymbol{x}},t),\ \widehat{\boldsymbol{x}}-\boldsymbol{x})\mathrm{d}V_{\widehat{x}} + \boldsymbol{f}_b(\boldsymbol{x},t) \tag{1}$$

where $\boldsymbol{u}$ is the displacement field, and ρ denotes the mass density. The domain H_x (see Fig. 1) is the so-called "horizon region" or simply "horizon" of material point $\boldsymbol{x}$, and here, in 2D, we take it to be a circular disk with radius δ (i.e. horizon size). The meaning, selection, and use of the peridynamic horizon and its practical application in modeling are detailed in Bobaru and Hu (2012). The integrand $\boldsymbol{f}$ is the pairwise force (*PD force or bond force*) in a peridynamic bond connecting material points $\boldsymbol{x}$ and $\widehat{\boldsymbol{x}}$, where $\widehat{\boldsymbol{x}}$ is a point in domain H_x (see Fig. 1). $V_{\widehat{x}}$ is the volume of the material point $\widehat{\boldsymbol{x}}$ covered by the horizon of $\boldsymbol{x}$. In this work, we focus on static problems, and the inertial term in Eq. (1) is ignored. For every material point, the body force, $\boldsymbol{f}_b(\boldsymbol{x})$, is balanced by the resultant force of all peridynamic bonds connecting to point $\boldsymbol{x}$. External forces, including forces exerted on the boundary layer, can be considered as body forces. Note that in a finite PD body (shown in Fig. 1), material nodes in the boundary layer have partial horizons, leading to different effective

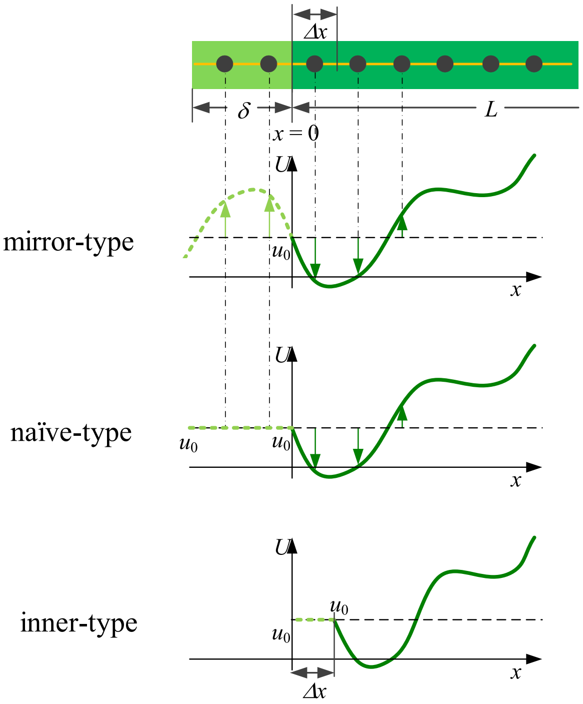

Fig. 3. Three types of imposing Dirichlet boundary conditions in a 1D PD model: mirror-type, naïve-type, and inner-type (redrawn from (Mei et al., 2021)).

mechanical properties from the bulk (with full horizon), if the material parameters have been calibrated using points in the bulk. We call this the surface effect of the PD model (Le and Bobaru, 2018).

The imposition of local boundary conditions in PD can also take different forms. Fig. 2 shows the comparison between surface traction in the classical model and the PD model. The surface traction ($\boldsymbol{T}_o$) at location $\boldsymbol{x}_o$ in the classical model is replaced by body forces in the surface layer ($\boldsymbol{F}_o(\boldsymbol{x})$) distributed along the normal direction ($\boldsymbol{n}$) at location $\boldsymbol{x}_o$. In the PD simulation, the surface layer has thickness δ (see Fig. 2). $\boldsymbol{T}_o$ and $\boldsymbol{F}_o(\boldsymbol{x})$ have the following relationship: $\boldsymbol{T}_o = \int_{\boldsymbol{x}_o}^{\boldsymbol{x}_o+\boldsymbol{n}\delta} \boldsymbol{F}_o(\boldsymbol{x})\mathrm{d}\boldsymbol{x}$. For simplicity, $\boldsymbol{F}_o(\boldsymbol{x})$ is assumed here to be uniformly distributed. Then, we have, $\boldsymbol{F}_o(\boldsymbol{x}) = \boldsymbol{T}_o/\delta$.

To impose Dirichlet-type boundary conditions in the PD model, three possible options are shown in Fig. 3, the first two belonging to the class of “fictitious nodes methods (FNM)”: mirror-type (displacement field in the fictitious domain is related by mirror symmetry to the corresponding domain in the deformable body), naïve-type (displacement field in the fictitious layer is constant and equal to the value of the local Dirichlet condition), and inner-type (displacement field in a finite layer inside the domain is fixed to be the local boundary temperature). While there is a single problem defined by the PD equation and the local boundary conditions we aim to enforce, these different implementations of such conditions would correspond, in general, to slightly different nonlocal problems: the PD equation and different associated nonlocal boundary conditions (or “volume constraints”). This means that for a fixed horizon, taking *m* (the ratio between the horizon size and the grid spacing) to go to infinity (*m*-convergence, (Bobaru et al., 2009)) in solving the PD equation with the local B.C. imposed using one of the options above could reach slightly different nonlocal solutions. Note that even if no surface correction methods are used in a peridynamic model, and local BCs are directly applied at the boundary nodes, the PD solution would still converge to the classical solution in the limit of the horizon size going to zero (Chen et al., 2016; Jha and Lipton, 2019).

In this work, we use the mirror-type Fictitious Nodes Method (FNM) for imposing classical Dirichlet BCs on the nonlocal model. Appendix A gives more details on the mirror-type FNM. Traction BCs are applied directly as body forces onto the fictitious nodes layer, for simplicity (as shown in Fig. 2), instead of using the FNM which would translate traction BCs into constrained displacements for the fictitious nodes. Therefore, for the wavy crack surfaces shown in Part II of this work (Dong et al., al.), we do not need to calculate the normal vector along the crack surface, since crack surfaces are considered traction-free.

Here, $\boldsymbol{\xi} = \widehat{\boldsymbol{x}} - \boldsymbol{x}$ denotes the relative reference position between nodes $\boldsymbol{x}$ and $\widehat{\boldsymbol{x}}$, $\boldsymbol{\eta} = \boldsymbol{u}(\widehat{\boldsymbol{x}}, t) - \boldsymbol{u}(\boldsymbol{x}, t)$ is the relative displacement, and thus $\boldsymbol{\xi} + \boldsymbol{\eta}$ represents the relative position between the nodes in the current configuration. Depending on the required horizon-scale behavior, the pairwise force $\boldsymbol{f}$ can take different forms Chen et al. (al.). For a microelastic material, the pairwise force is given as:

$$f(\boldsymbol{\eta},\boldsymbol{\xi}) = \begin{cases} \dfrac{\boldsymbol{\xi}+\boldsymbol{\eta}}{\boldsymbol{\xi}+\boldsymbol{\eta}} c(\boldsymbol{\xi}) s & \xi \leq \delta \\ 0 & \xi > \delta \end{cases} \tag{2}$$

where $s = \frac{\eta+\xi-\xi}{\xi}$, is the bond relative elongation. $c(\boldsymbol{\xi})$, a coefficient of elasticity, is the micro-modulus in the PD model. The micro-modulus function can take different forms, depending on the required horizon-scale behavior. Here we only consider the constant-profile micro-modulus function (independent of the bond length), which, when we set up a match of the strain energy density with the classical theory for a homogeneous deformation, leads to the following forms:

$$c(\boldsymbol{\xi}) = \begin{cases} \dfrac{9E}{\pi\delta^3}, & \text{plane stress} \\ \dfrac{48E}{5\pi\delta^3}, & \text{plane strain} \end{cases} \tag{3}$$

in 2D. Here E is the Young's modulus.

Eq. (2) assumes a linear constitutive relationship. When the peridynamic bond crosses a dislocation slip plane, a plastic slip needs to be considered in the constitutive relation. Following Section 3 shows the way we deal with bond crossing slip planes in the PD model.

The peridynamic bonds can break irreversibly, or reversibly when they are meant to represent, for example, van der Waals-like interactions (Silling and Bobaru, 2005). For irreversible bond breaking, if the bond elongation excesses a critical bond strain, we have $\boldsymbol{f}(\boldsymbol{\xi},\boldsymbol{\eta}) = 0$. The critical bond strain s_0 is calibrated to the material's fracture energy G_0, for the micro-modulus functions given above, as follows:

$$G_0 = 2\int_0^\delta \int_z^\delta \int_0^{\cos^{-1}\left(\frac{z}{r}\right)} \left[\frac{cs_0^2 r}{2}\right] r\mathrm{d}\theta\mathrm{d}r\mathrm{d}z \tag{4}$$

Consequently, we have:

$$s_0 = \begin{cases} \sqrt{\dfrac{4\pi G_0}{9E\delta}}, & \text{plane stress} \\ \sqrt{\dfrac{5\pi G_0}{12E\delta}}, & \text{plane strain} \end{cases} \tag{5}$$

Damage evolution and crack propagation are studied in Part II of this work (Dong et al., al.). The discretization and numerical algorithms for solving the static version of Eq. (1) are summarized in Appendix B.

In the current DDD framework, dislocation nucleation and motion are related to stresses. It is critical to calculate the stress distribution. The peridynamic stress tensor can be defined as (Lehoucq and Silling, 2008):

$$\boldsymbol{\nu}(\boldsymbol{x}) = \frac{1}{2}\int_{\mathscr{S}}\int_0^\infty\int_0^\infty (y+z)^2 \boldsymbol{f}(\boldsymbol{\eta},\boldsymbol{\xi}) \otimes \boldsymbol{q}\mathrm{d}z\mathrm{d}y\mathrm{d}\Omega_{\boldsymbol{m}} \tag{6}$$

where $\mathscr{S}$ is the unit sphere, $\mathrm{d}\Omega_{\boldsymbol{q}}$ is a differential solid angle on $\mathscr{S}$ in the direction of any unit vector $\boldsymbol{q}$ and

$$\boldsymbol{\eta} = \boldsymbol{u}(\boldsymbol{x}+y\boldsymbol{q}) - \boldsymbol{u}(\boldsymbol{x}-z\boldsymbol{q}), \quad \boldsymbol{\xi} = (\boldsymbol{x}+y\boldsymbol{q}) - (\boldsymbol{x}-z\boldsymbol{q}) \tag{7}$$

Then, according to (Lehoucq and Silling, 2008), the formula below holds when $\boldsymbol{f}$ is continuously differentiable:

$$\nabla\cdot\boldsymbol{\nu}(\boldsymbol{x}) = \int_{H_x} \boldsymbol{f}(\boldsymbol{u}(\boldsymbol{x},t) - \boldsymbol{u}(\widehat{\boldsymbol{x}},t),\ \widehat{\boldsymbol{x}} - \boldsymbol{x})\mathrm{d}V_{\widehat{\boldsymbol{x}}} \tag{8}$$

The peridynamic equation of motion can be thus rewritten as

$$\rho(\boldsymbol{x})\ddot{\boldsymbol{u}}(\boldsymbol{x},t) = \nabla\cdot\boldsymbol{\nu}(\boldsymbol{x}) + \boldsymbol{f}_{\boldsymbol{b}}(\boldsymbol{x},t) \tag{9}$$

which is formally identical to the equation of motion in the classical theory. In addition, (Silling and Lehoucq, 2008) points out that $\boldsymbol{\nu}(\boldsymbol{x})$ converges as $\delta \to 0$. Hence, when $\delta \to 0$, peridynamics is identical to classical theory in constitutive model of which the stress tensor $\boldsymbol{\sigma}(\boldsymbol{x}) = \boldsymbol{\nu}(\boldsymbol{x})$ for all continuous displacement fields $\boldsymbol{u}(\boldsymbol{x})$. Appendix C shows the algorithms to compute stresses at a discretized nodal point. Stresses at other locations are obtained by interpolation from the nodal values.

When computing stresses near boundaries, we use the same formula as Eq. (6) since the PD output (displacements) has already been corrected with the use of the FNM. Note also traction-free crack surfaces are treated as discussed for traction-free surfaces.

In numerical simulations, the calculated stress depends on the discretization grid and the horizon size, which imply discretization errors, and differences between the nonlocal and corresponding local solutions. It may be possible to develop new ways to calculate highly-accurate (closer to the classical solution) stresses from PD models, and also formulate new models for dislocation evolution

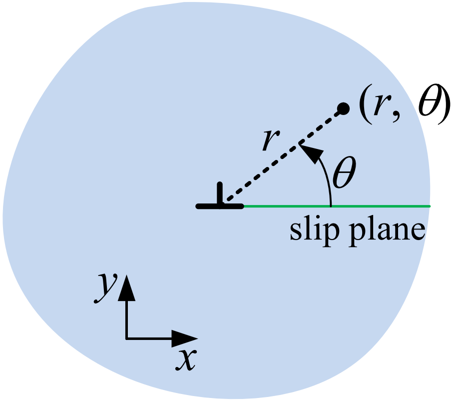

Fig. 4. Schematic of an edge dislocation.

based on deformations or displacements only, without the need to calculate stresses in the PD model. This will be studied in the future.

3. The DDD-PD frameworks for plastic deformations

In this section, we briefly review the discrete-continuous (DC) scheme and introduce the new superposition (SP) scheme for 2D DDD-PD simulations of plastic deformation induced by dislocations. The major difference of the DDD-PD model from the PD model without considering the dislocations in a DDD module is the displacement jump across a dislocation slip plane and the constitutive relation for PD bonds when they are crossed by dislocation slips. We show this model in Section 3.2, after a brief introduction of the DDD theory in Section 3.1.

3.1. Brief introduction of dislocation theory

Before presenting the DDD-PD frameworks, we briefly review the basic dislocation theory in this subsection. In classical 2D DDD models, dislocations are treated as line defects in the elastic continuum induced by atomic slip (Anderson et al., 2017). Each dislocation is characterized by a Burgers vector, which is defined as the value of the relative elastic distortion displacement around the dislocation core and is usually indicated by the symbol $\boldsymbol{b}$.

Depending on the angle between the dislocation line and the direction of the Burgers vector, dislocations can be divided into three categories. When this angle is 90° (i.e., a dislocation line perpendicular to the direction of Burgers vector), the dislocation is called an "edge dislocation". When the angle is zero, i.e., dislocation line is parallel to the direction of Burgers vector, we have a "screw dislocation". In all other cases we are dealing with a "mixed dislocation". In this 2D work, we only focus on edge dislocations, but the procedure introduced in this paper can be applied for other types of dislocations.

According to the dislocation theory (Anderson et al., 2017; Van der Giessen and Needleman, 1995), the stress field and deformation field of dislocations in an infinite body can be expressed as a superposition of the fields for each individual dislocation:

$$\widetilde{\boldsymbol{u}} = \sum_{i=1,2\ldots}^{n} \boldsymbol{u}_i, \widetilde{\boldsymbol{\varepsilon}} = \sum_{i=1,2\ldots}^{n} \boldsymbol{\varepsilon}_i, \widetilde{\boldsymbol{\sigma}} = \sum_{i=1,2\ldots}^{n} \boldsymbol{\sigma}_i \tag{10}$$

where n is the number of dislocations. $\boldsymbol{u}_i$, $\boldsymbol{\varepsilon}_i$, $\boldsymbol{\sigma}_i$, are displacement, strain and stress fields induced by the i th dislocation, respectively. For plane-strain problems, the stress and displacement fields induced by an edge dislocation (see Fig. 4) can be expressed analytically as Anderson et al. (2017):

$$\begin{cases} \widetilde{\sigma}_{rr} = -\dfrac{\mu b}{2\pi r(1-\nu)}\sin\theta \\ \widetilde{\sigma}_{\theta\theta} = -\dfrac{\mu b}{2\pi r(1-\nu)}\sin\theta \\ \widetilde{\sigma}_{r\theta} = \dfrac{\mu \mathrm{b}}{2\pi r(1-\nu)}\cos\theta \end{cases} \tag{11}$$

$$\begin{cases} \widetilde{u}_x = \dfrac{b}{2\pi(1-\nu)}\left[(1-\nu)\theta + \dfrac{\sin 2\theta}{4}\right] \\ \widetilde{u}_y = -\dfrac{b}{2\pi(1-\nu)}\left[\dfrac{1-2\nu}{2}\ln r + \dfrac{\cos 2\theta}{4}\right] \end{cases} \tag{12}$$

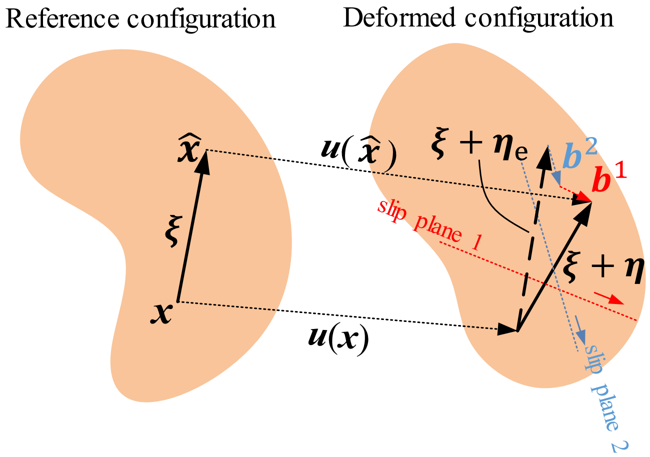

Fig. 5. Elasto-plastic deformation of peridynamic bond crossing dislocation slip planes. In the deformed state, two slip planes cross the peridynamic bond x-$\hat{x}$.

where (r, θ) are the polar coordinates, with the dislocation located at the origin and the slip plane acting along the line $\theta = 0$ (see Fig. 4). μ and ν are the material shear modulus and Poisson's ratio, respectively. b is the magnitude of the Burgers vector. On the slip plane, we have, $\tilde{u}_x(\theta = 2\pi) = \tilde{u}_x(\theta = 0) + b$, i.e., a displacement discontinuity exists along the slip plane $\theta = 0$.

The movement of dislocations depends on their Peach-Koehler (PK) forces (Peach and Koehler, 1950). In DDD, the short-range effects on dislocations, such as dislocation nucleation, annihilation, hinderment, etc., are represented by a set of constitutive laws. The evolution of dislocations is investigated in Part II of this work (Dong et al., al.), while here, in Part I of this work, we focus on problems with stationary dislocations and their interactions with voids, cracks, and other dislocations.

3.2. PD bonds crossing dislocation slip planes

Consider a PD bond connecting x and $\hat{x}$ as shown in Fig. 5. The bond relative position ξ changes to $\xi + \eta$, after the structure is deformed. If dislocation crosses the bond x-$\hat{x}$, its deformation is purely elastic and the bond elastic strain is $\frac{\eta + \xi - \xi}{\xi}$. However, if the deformed configuration contains slip planes crossing the peridynamic bond x-$\hat{x}$, its deformation is no longer purely elastic. For instance, if two slip planes cross the peridynamic bond, as shown in Fig. 5, in the DDD-PD model, the elastic part of the bond strain changes to:

$$s_e = \frac{\eta_e + \xi - \xi}{\xi} \tag{13}$$

where $\eta_e + \xi = \eta + \xi - \sum_i b^i$. Here b^i is the Burgers vector of the i th dislocation shown in Fig. 5. In this model, plastic deformation can only exist at material points with peridynamic bonds crossed by dislocation slip planes.

Note that for a finite horizon size, a dislocation in the model has a thickness related to the horizon size. In the limit of the horizon size going to zero, the width of the PD dislocation goes to zero and we approach the mathematical slip plane (zero thickness) in the classical model. In reality, slip planes do not have a zero thickness and dislocations affect the material through a certain thickness across the slip plane. Therefore, a nonlocal representation of dislocations is justified from a physical point of view. While the PD model could be used as a molecular dynamics simulation, the goal is to have it as a continuum model at the micrometer scale, and thus the horizon size does not have to match the physical range of effects induced by a slip plane in a crystal. In the future, we will compare the continuum-based DDD-PD model with molecular dynamics, to further verify the DDD-PD model, and to provide a more comprehensive understanding of the plastic deformation and fracture of crystalline metals.

In numerical PD computations, we need to differentiate the bonds intersected by dislocation slips from those without any crossings. The algorithm used to determine whether a bond is crossed by a dislocation slip is shown in Appendix B.

The discrete-continuous (DC) scheme of DDD-PD recently reported in Zhao and Shen (2021), embedded the discontinuities of dislocation slips directly into the PD constitutive law. The DC DDD-PD coupling framework does not use the analytical solutions (where stress singularities appear) of the dislocation stress and displacements in the infinite domain. Only the locations of dislocation slip planes and the magnitude of the plastic deformation need to be introduced on both sides of the slip plane for the PD calculation. The DC scheme's deficiency is that its accuracy depends highly on the distance from the dislocation core. In the example of dislocation interaction in (Zhao and Shen, 2021), the distance between two dislocation cores is far larger than the horizon size. However, during the plastic deformation and fracture of metallic materials, the dislocation-dislocation, dislocation-crack, dislocation-damage and (or) dislocation-interface interactions are inevitable, meaning that the DC scheme may have trouble modeling dislocation-based plasticity. It is not immediately clear if the DC-PD scheme is applicable to simulating dislocation evolution, since their interactions cannot be

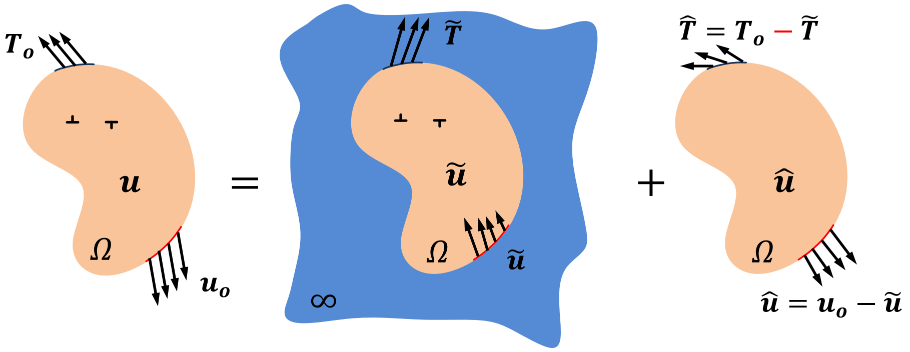

Fig. 6. Schematic diagram of DDD in the superposition (SP) scheme in classical continuum mechanics framework. Redrawn from (Van der Giessen and Needleman, 1995).

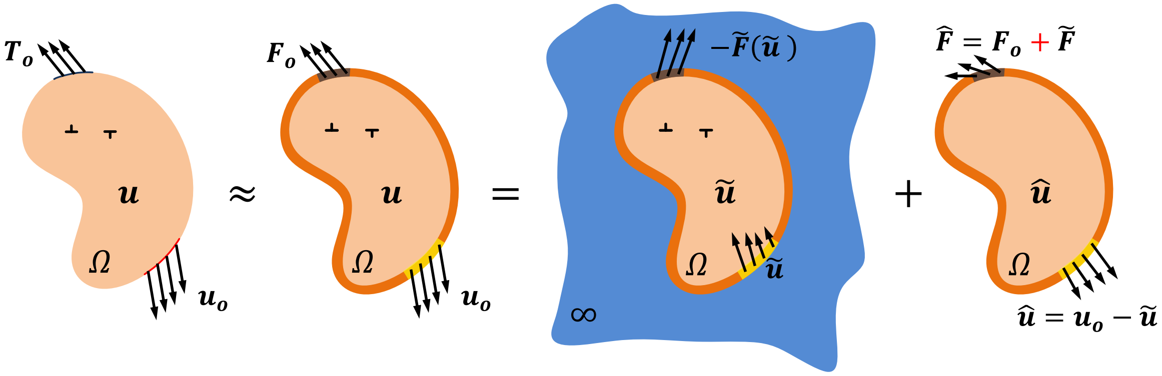

Fig. 7. Schematic diagram for the SP DDD-PD model.

calculated accurately when they are close enough. This likely makes the DC DDD-PD scheme inapplicable to simulating dislocation-based plasticity, since dislocations would artificially become stuck at boundaries or stuck between themselves.

To overcome this issue, in the next section, we introduce the superposition (SP)-PD scheme, in which dislocation fields are superposed on the peridynamic elastic field. In the numerical examples, we will see that the SP scheme can handle the cases with dislocations close to boundaries or other dislocations.

3.3. *The superposition (SP) scheme for the DDD-PD model*

In the present SP DDD-PD scheme for boundary value problems (BVPs), the stress, strain and displacement fields are written as superpositions of discrete dislocation fields (Eq. (10)) and complementary fields (Van der Giessen and Needleman, 1995) as is done in the classical approach:

$$\boldsymbol{u} = \widetilde{\boldsymbol{u}} + \widehat{\boldsymbol{u}}, \quad \boldsymbol{\varepsilon} = \widetilde{\boldsymbol{\varepsilon}} + \widehat{\boldsymbol{\varepsilon}}, \quad \boldsymbol{\sigma} = \widetilde{\boldsymbol{\sigma}} + \widehat{\boldsymbol{\sigma}} \tag{14}$$

where the tilde ($\sim$) represents the analytical dislocation fields in an isotropic infinite domain, and the hat ($\wedge$) stands for the complementary elastic field to satisfy the boundary conditions. The complementary fields have been computed by numerical solutions to the BVPs described by PDEs, such as the FEM, XFEM, Phase-field, etc. The main difference between the classical DDD models and the DDD-PD ones is in representing the complementary problem as an integro-differential problem with associated nonlocal boundary constraints. As shown in Fig. 6, the traction and displacement boundary conditions of the amendment problem, i.e., the ($\wedge$) field, can be expressed as:

$$\begin{aligned} \widehat{\boldsymbol{T}} &= \boldsymbol{T}_0 - \widetilde{\boldsymbol{T}}, \quad \text{on the traction boundary} \\ \widehat{\boldsymbol{u}} &= \boldsymbol{u}_0 - \widetilde{\boldsymbol{u}}, \quad \text{on the displacement boundary} \end{aligned} \tag{15}$$

where the $\{\boldsymbol{T}_0, \boldsymbol{u}_0\}$ are the actual given boundary conditions for the problem. In addition, as indicated in Fig. 6, $\{\widetilde{\boldsymbol{T}}, \widetilde{\boldsymbol{u}}\}$ are the tractions and displacements on the boundaries of the actual domain induced by all dislocations embedded in the infinite body.

Classical models face difficulties in solving problems with damage, fracture, etc. (in which the crack paths, for example, are not known in advance), because of the presence of mathematical singularities at corners, crack-tips, dislocations, the need for external ad-

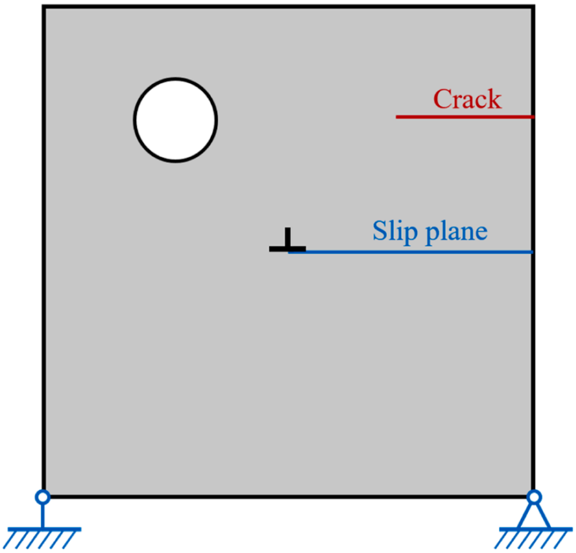

Fig. 8. A 2D square plate with an edge dislocation, a circular void, and an edge crack.

hoc rules for the evolution of such defects, and the need for tracking of interfaces/cracks/boundaries as they evolve. It is worth to mention that in dislocation-based studies of elastoplastic fracture, fracture paths are generally preset, e.g., as straight segments (Liang et al., 2019). However, experimental evidence shows tortuous fracture surfaces in single crystals (Creuziger et al., 2008; Kalácska et al., 2020; Sumigawa et al., 2018). PD formulations handle these difficult problems by eliminating singularities from the mathematical model and embedding simple bond-damage rules (mapped to physical failure criteria, e.g. Griffiths fracture), general enough to be able to reproduce, autonomously, complex evolution paths for damage or crack propagation, without any explicit tracking of interfaces/cracks/boundaries, which are implicit in these models. Moreover, PD models allow for integrating possible nonlocal effects induced by dislocations/microstructure/damage and their evolution. We apply the classical DDD superposition framework for the PD formulation of DDD, and the main differences are explained below.

The replacement of the classical complementary problem with a nonlocal one leads to important changes (the schematic diagram of the proposed SP DDD-PD framework is provided in Fig. 7). A plane-strain 2D elastoplastic problem with boundary tractions $\boldsymbol{F_0}$ and displacement boundary condition $\boldsymbol{u_0}$ is considered. Similar to the superposition scheme for the DDD-FEM method, the deformation fields for the SP DDD-PD method are also decomposed into ($\sim$) and ($\wedge$) parts, as illustrated in Eq. (14). For the classical SP DDD framework shown in Fig. 6, the boundary tractions $\widetilde{\boldsymbol{T}}$ induced by dislocations are calculated from the analytical dislocation stress formula given in Eq. (11). However, the proposed SP DDD-PD framework calculates the complementary traction $\widetilde{\boldsymbol{F}}(\widetilde{\boldsymbol{u}})$ by substituting the dislocation displacement field $\widetilde{\boldsymbol{u}}$ (the analytical solution in the infinite domain) into the PD formulation (Eq. (1)). As shown in Fig. 7, in the DDD solution for the infinite domain, the displacement field ($\widetilde{\boldsymbol{u}}$) calculated over the finite domain is used to compute the *boundary traction* $-\widetilde{\boldsymbol{F}}(\widetilde{\boldsymbol{u}})$. As a result, the boundary conditions for the complementary part of the problem can be written as:

$$\widehat{\boldsymbol{F}} = \boldsymbol{F}_0 + \widetilde{\boldsymbol{F}}(\widetilde{\boldsymbol{u}}), \quad \widehat{\boldsymbol{u}} = \boldsymbol{u}_0 - \widetilde{\boldsymbol{u}} \tag{16}$$

Since $\widetilde{\boldsymbol{u}}$ is a static solution, in the classical model, $\widetilde{\boldsymbol{F}}(\widetilde{\boldsymbol{u}})$ should be zero at all points. This is, however, not true for a nonlocal model because of the PD surface effect. Indeed, for static BVPs with dislocations, the integral in the PD equation (Eq. (1)) is zero (static equilibrium) at a point with a full horizon (away from the boundary) and without any of its bonds damaged. However, if the considered point is near a boundary, a material interface, or has any of its bonds damaged, the integral (i.e., body force) is no longer zero: this is the PD surface effect (see (Le and Bobaru, 2018)). These non-zero resultant bond forces ($-\widetilde{\boldsymbol{F}}(\widetilde{\boldsymbol{u}})$), functions of the analytical dislocation displacement field $\widetilde{\boldsymbol{u}}$, are used as input (applied as a body force over the nonlocal boundary where tractions are applied, added to the given $\boldsymbol{F}_0$) for solving the complementary problem (see Fig. 7) for the displacement field $\widehat{\boldsymbol{u}}$. Once this PD problem is solved, we have the displacement field $\boldsymbol{u}$ (see Eq. (14)).

The key difference between the classical SP scheme and the present SP DDD-PD scheme is the replacement of the local model in the complementary problem with a nonlocal/peridynamic one. We can also apply the same procedure used in the traditional SP approach for the PD model. However, in this way, we will encounter the same issues faced by the traditional SP approach that we need to explicitly track boundaries, interfaces, cracks, etc., and obtain the normal directions for all of the surfaces/interfaces, which may be not exist at corners, for example. In particular, nonlocal interactions (applied as body forces) are used to replace the classical surface tractions (on the complementary problem traction-boundary), which eliminates the need for explicitly tracking boundaries, interfaces, cracks, etc., and makes the model very general and flexible. In the current PD framework, the traction (including traction-free) boundaries, cracks, damaged regions, and voids are treated in a united way (in PD, tractions are implemented via body forces).

Note, however, that the classical analytical dislocation displacement (given in Eq. (12)) leads to a stress singularity at the

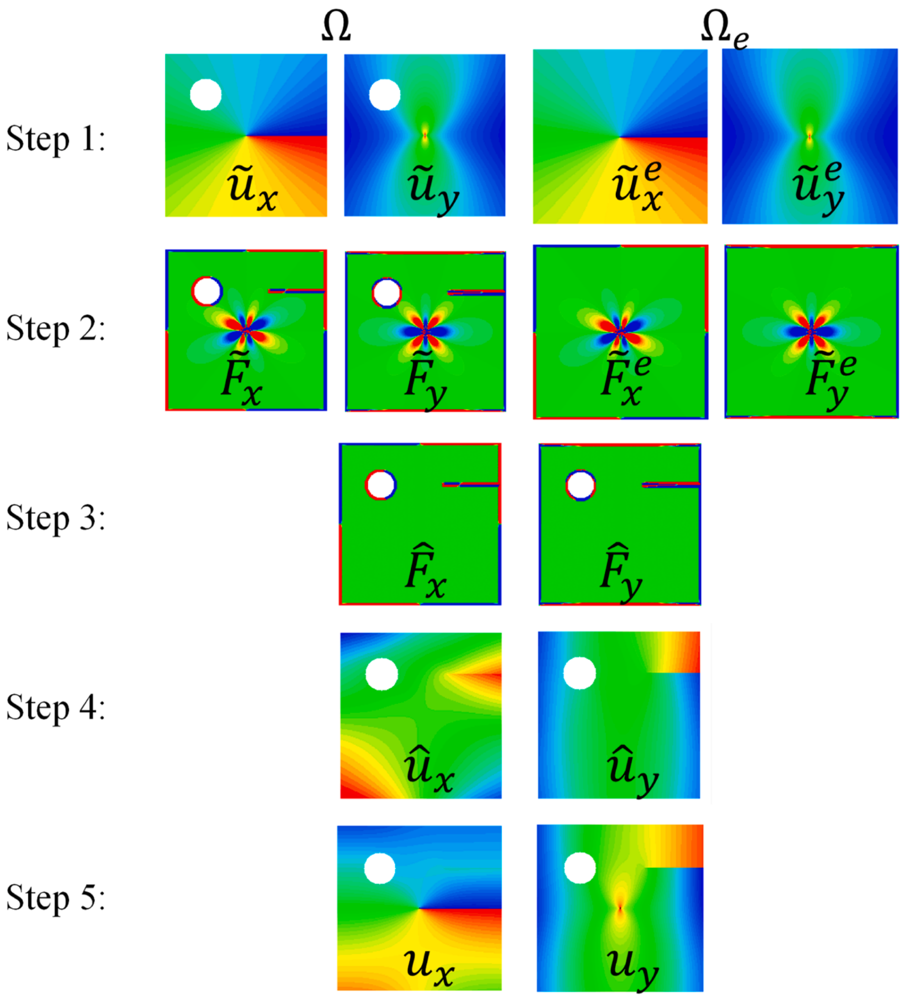

Fig. 9. Outputs from each of the steps in the SP scheme of the DDD-PD model for the problem shown in Fig. 8. The color represents the magnitude of each quantity plotted.

dislocation core. Any numerical approximation method for this problem would incur errors, especially around the dislocation core (see Appendix D for details), and, as a result, the force at nodes near the dislocation core (computed from Eq. (1): $\widetilde{\boldsymbol{F}} = \int_{H_x} \boldsymbol{f}(\boldsymbol{u}(\boldsymbol{x},t) - \boldsymbol{u}(\widehat{\boldsymbol{x}},t), \widehat{\boldsymbol{x}} - \boldsymbol{x})\mathrm{d}V_{\widehat{x}}$) will not be zero even if these material points are away from the surface boundary and they have no damaged bonds. In order to eliminate this numerical error (the non-zero resultant nodal forces induced by the numerical approximation of Eq. (1)) near the dislocation cores, we can subtract a similar PD force field (corresponding to the analytical solution over the infinite domain) but computed on a slightly larger PD domain, Ω_e, containing the given finite domain, in which all points in Ω now have a full horizon contained in the Ω_e. The extended domain, Ω_e will contain only the dislocation cores, but none of the defects/cracks/voids, that Ω might have. Subtracting these computed PD force fields from one another would lead to perfectly equilibrated forces around the dislocation cores, and also provide us with the traction forces that need to be applied in the complementary problem (on its boundaries and at defects, if present). In PD tractions are applied as body forces, and for points in the bulk and with zero damage in Ω these forces would be zero, and non-zero over the layer of thickness δ inside Ω and at points that have some damage or incomplete horizons.

Because of the use of the extended domain, there is no need to explicitly identify and track boundaries or locations of defects, since a non-zero resultant force $\widetilde{\boldsymbol{F}} - \widetilde{\boldsymbol{F}}^e$ implicitly indicates a surface node (proximity to the boundary), or a node with damage or on a crack surface or near a material interface.

A step-by-step explanation of the SP DDD-PD model is given below for a typical configuration, shown in Fig. 8. The domain Ω_e can be selected, for example, as an extension of the original domain Ω with a collar of thickness δ all around its boundary. In practice, the extra nodes the extended domain has compared to the original, are simply appended as "supplementary nodes" to the existing nodal data structure for Ω. Once a numerical grid is generated for Ω and Ω_e domains, the SP DDD-PD algorithm is as follows (see Fig. 9 for the results corresponding to each step):

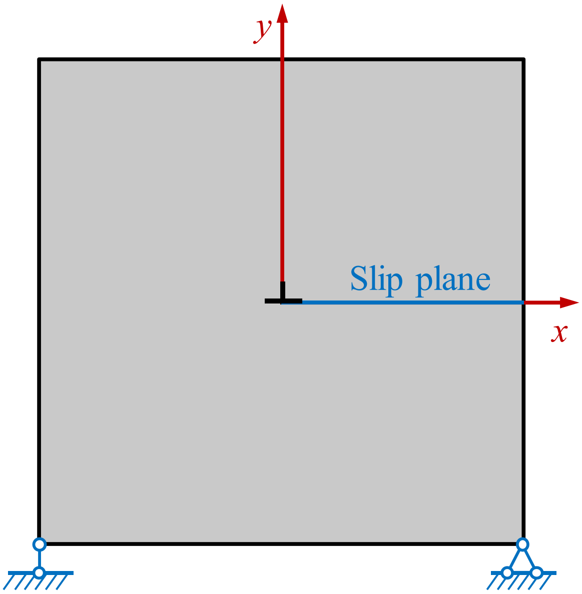

Fig. 10. Domain, dislocation position, and boundary conditions for the single slip plane case.

Step 1: Calculate the displacement field $(\widetilde{u}_x, \widetilde{u}_y)$ from the analytical solution for the embedded dislocations in the infinite domain at all nodes in the given finite domain (Ω) from Eq. (12). Similarly, calculate the displacement field $(\widetilde{u}_x^e, \widetilde{u}_y^e)$ in the extended finite domain (Ω_e).
Step 2: Using the displacements in Step 1, compute the resultant PD forces on all nodes in both the original domain $(\widetilde{F}_x, \widetilde{F}_y)$ and the extended domain $(\widetilde{F}_x^e, \widetilde{F}_y^e)$ according to the PD Eq. (1): $\widetilde{\boldsymbol{F}} = \int_{H_x} \boldsymbol{f}(\boldsymbol{u}(\boldsymbol{x},t) - \boldsymbol{u}(\widehat{\boldsymbol{x}},t),\ \widehat{\boldsymbol{x}} - \boldsymbol{x})\mathrm{d}V_{\widehat{x}}$.
Step 3: Construct the body force to be applied in the complementary problem: at all nodes in domain Ω set $\widetilde{F}_x = \widetilde{F}_x - \widetilde{F}_x^e$ and $\widetilde{F}_y = \widetilde{F}_y - \widetilde{F}_y^e$ (to eliminate the numerical error induced by the non-zero resultant nodal forces near the dislocation cores). Evaluate the complementary bond forces $(\widehat{F}_x, \widehat{F}_y)$ for all the nodes in the domain Ω, according to Eq. (16). Calculate $(\widehat{u}_x, \widehat{u}_y)$ on the nodes on the displacement boundary according to Eq. (16), using $(\widetilde{u}_x, \widetilde{u}_y)$ obtained in Step 1.
Step 4: Solve the complementary PD problem by finding the PD displacements in Ω (solve Eq. (1) using, e.g., the nonlinear conjugate gradient method, see Appendix B) for the data computed in Step 3 (applied body forces and applied boundary displacements).
Step 5: Obtain the total displacement field (u_x, u_y) by superposition of $(\widehat{u}_x, \widehat{u}_y)$ and $(\widetilde{u}_x, \widetilde{u}_y)$. Compute stress distribution using the algorithms shown in Appendix C.

The discrete-continuous (DC) DDD-PD coupling framework does not use the analytical solutions Eqs. (11) and ((12)) of the dislocation stress and displacement in the infinite domain (Zhao and Shen, 2021). Only traces of dislocation slips and the magnitude of the plastic deformation need to be introduced on both sides of the slip plane for the PD calculation. While simple, the DC scheme's deficiency is that its accuracy depends highly on the distance from the dislocation core. When two dislocations are close enough, their interaction cannot be accurately described by the DC scheme. However, during the plastic deformation and fracture of metallic materials, the dislocation-dislocation, dislocation-crack, dislocation-damage and (or) dislocation-interface interactions are inevitable, and using the DC scheme to model dislocation-based plasticity seems difficult. The new SP DDD-PD framework overcomes this issue because in the SP scheme the singularities at the dislocation cores are kept by the superposed analytical solutions. In the following sections, we verify the new model and compare results with the DC approach and DDD-FEM on a number of sample problems.

Note that in the SP DDD-PD framework, we superimpose the solution from the classical elasticity and the solution from nonlocal PD model. In the SP DDD-PD model, we treat the PD model as a numerical technique. It has been proved that the PD solution converges to the corresponding classical one at the limit $\delta \to 0$ (Chen et al., al., 2022; Jha and Lipton, 2019; Tian and Du, 2014). For the SP DDD-PD model, the solution should converge to the exact local solution in the limit of the horizon $\delta \to 0$.

4. Model verification and comparison with other models

In this section, we use the SP scheme for DDD-PD to solve four typical 2D plane-strain boundary value problems (BVPs): simply-supported 2D squares with a single dislocation, with multiple dislocations, with a dislocation emitted from the crack tip and with a dislocation close to a void, and a simply-supported cylinder with a single dislocation. The results are compared against analytical

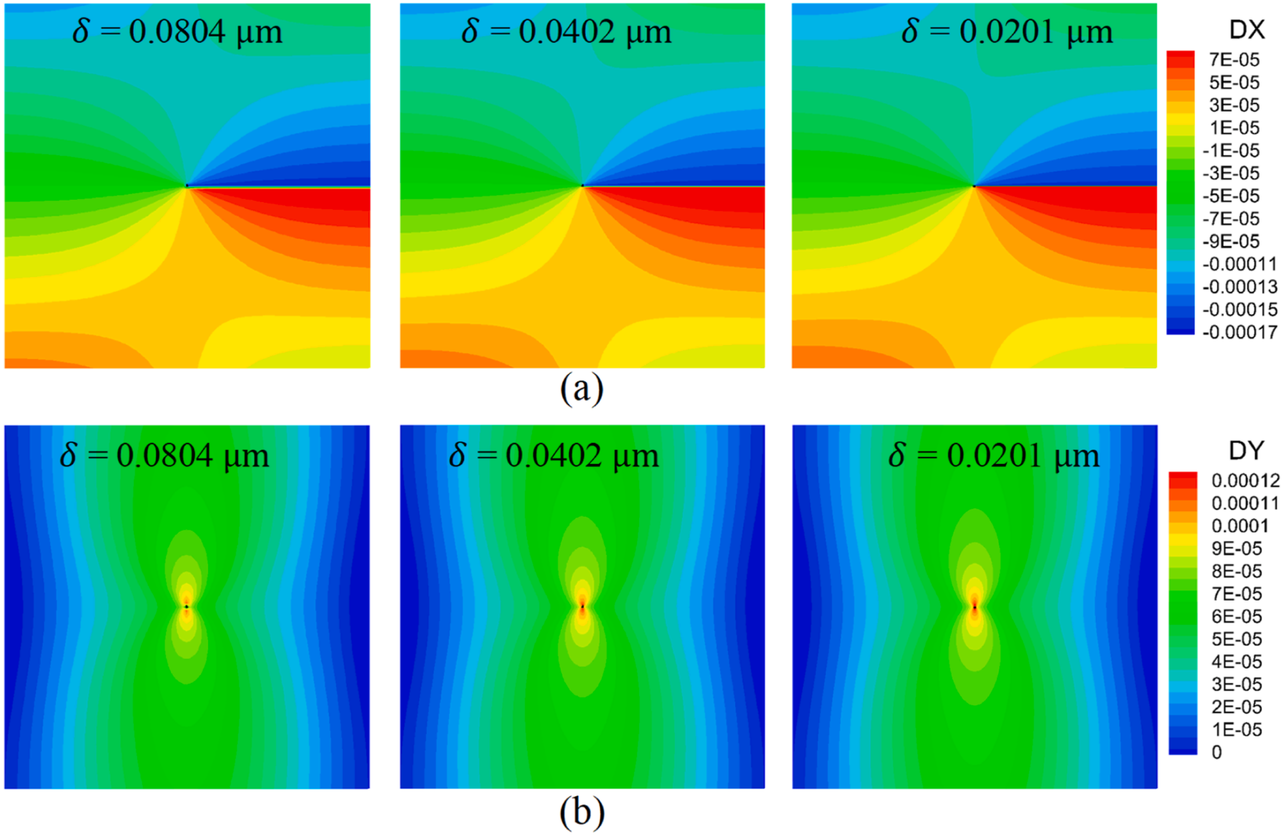

Fig. 11. (a) Horizontal and (b) vertical displacement distributions obtained by using the SP DDD-PD model, with different horizon sizes: $\delta = 0.0804$, 0.0402 and 0.0201 μm. The units of the values shown in the figure (displacements, coordinates, and horizon sizes) are μm. The same units are used in the similar remaining figures in the paper.

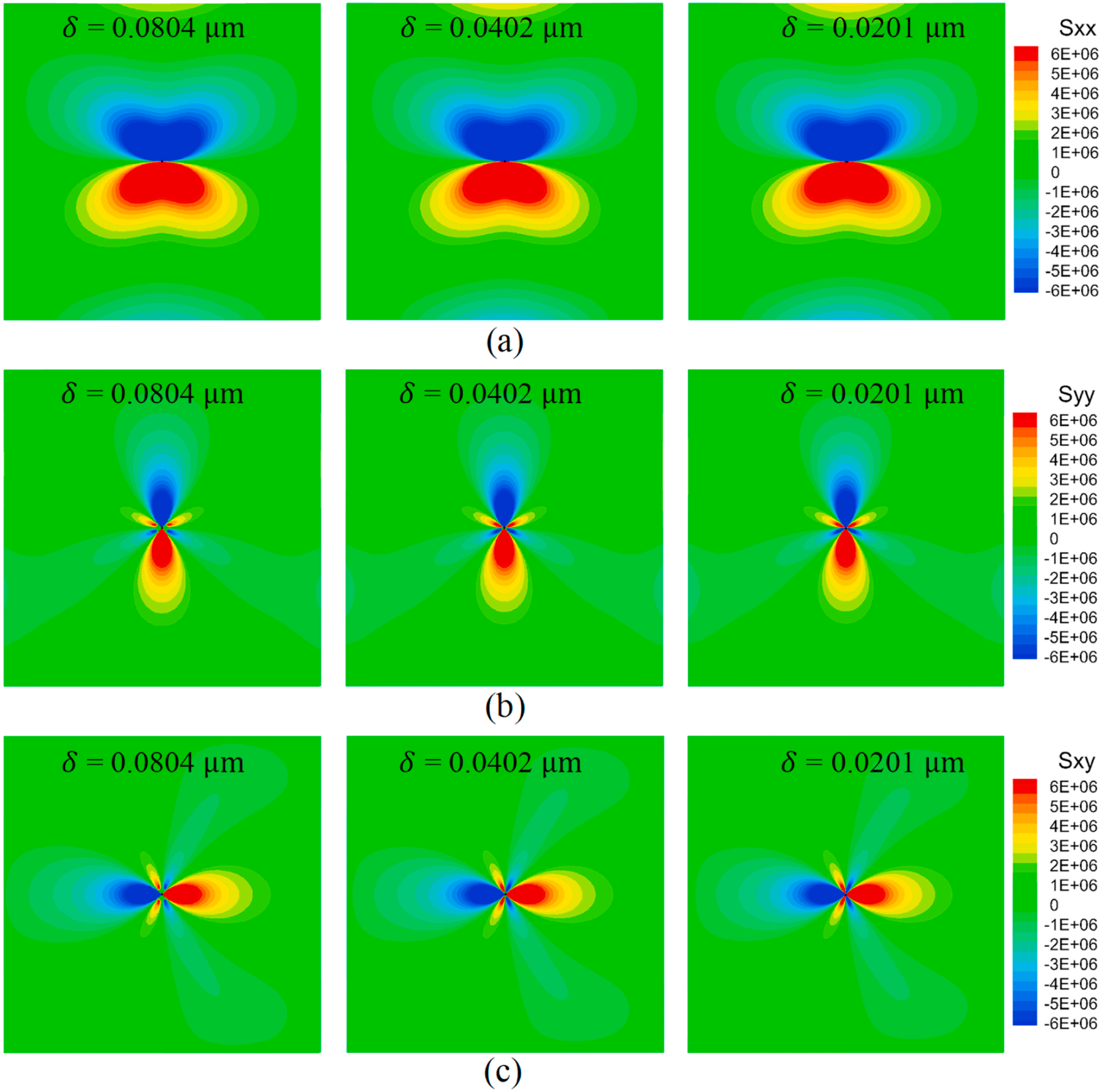

Fig. 12. Stresses (a) σ_{xx}; (b) σ_{yy}; (c) σ_{xy} obtained by using the SP DDD-PD model, with different horizon sizes: $\delta = 0.0804$, 0.0402 and 0.0201 µm. The unit for stresses is Pa (the same unit is used for stresses shown in the remaining figures).

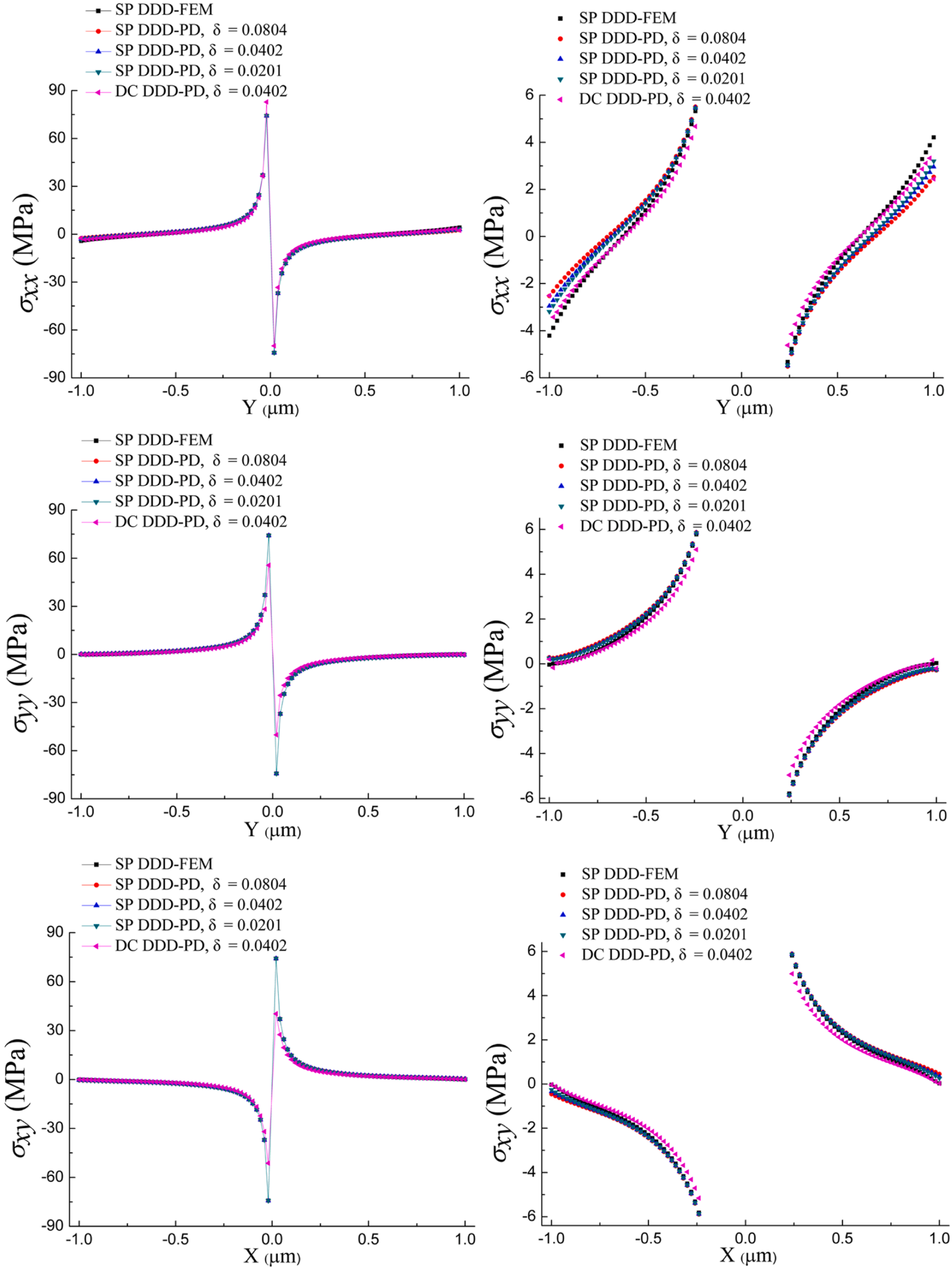

(caption on next page)

Fig. 13. Stress profiles from three DDD models (SP DDD-FEM, SP DDD-PD, and DC DDD-PD): σ_{xx} on $x = 0$ μm (top panels), σ_{yy} on $x = 0$ μm (middle panels) and σ_{xy} on $y = 0$ μm (bottom panels). The left panels show results over the full stress scale, while the right panels show the same results but on a narrower stress range to more clearly observe the differences between the different solutions near the domain boundaries.

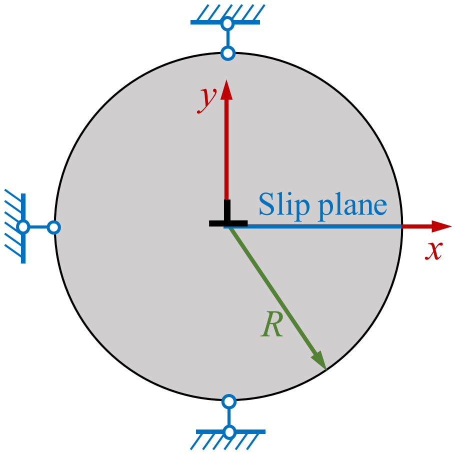

Fig. 14. Dislocation position and boundary conditions for the cylinder case.

solutions of the classical models, as well as against solutions we computed for these problems using the DC scheme for DDD-PD (following (Zhao and Shen, 2021)) and the SP scheme for DDD-FEM (following (Huang and Li, 2015)).

For all numerical cases considered in this paper, the material constants are set as Young's modulus $E = 70$ GPa, Poisson's ratio $\nu = 0.25$, and the magnitude of Burgers vector $b = 0.25$ nm for aluminum. 2D plane-strain state is considered.

4.1. BVP with single edge dislocation

4.1.1. Square domain solution

Consider a simply-supported (at two bottom corners as shown in Fig. 10) square crystal with a side length $L = 2$ μm. An edge dislocation is located at the center of the square. All the boundaries are traction free. The displacement boundary conditions (displacement constrained at the bottom two corners) are applied in a boundary layer of δ thickness. The mirror boundary treatment (Le and Bobaru, 2018; Mei et al., 2021) is adopted for solving the displacement boundary condition by PD. The corresponding extended domain for this problem is a square with a side length equaling to $2 + 2\delta$ μm. The mirror boundary treatment is applied in the PD modeling for all other examples shown in this paper.

The horizon factor (i.e., the ratio between horizon size and the grid spacing) is fixed at 4.02, which is a typical value for the horizon factor for the PD model with a uniform grid. Different horizon sizes $\delta = 0.0804$, 0.0402 and 0.0201 μm are applied to verify the PD calculation convergence, corresponding to 11,881, 43,681 and 167,281 nodes, respectively in the domain. Following the simulation steps given in Section 3.3, the BVP shown in Fig. 10 is solved, and the displacement and stress fields are plotted in Fig. 11 and Fig. 12, respectively. The displacement discontinuity across the slip plane and stress singularity at the dislocation core are well captured by the present SP DDD-PD framework. The results with different horizon sizes show that these horizons are sufficiently small for the nonlocal solutions to be very close to the classical solution, in both displacements and stress fields.

For comparison, the SP DDD-FEM algorithm is also applied to solve the same problem shown in Fig. 10. The corresponding displacement and stress results are given in Fig. 33 and Fig. 34 (in Appendix E), respectively, for the element size 0.01 μm, which equals the grid spacing of the above PD model with horizon size 0.0402 μm. It is clearly shown that the results of the SP DDD-PD model and the DDD-FEM model are consistent with each other. To quantitatively analyze the computation accuracy, the stress results obtained by SP DDD-FEM, SP DDD-PD and DC DDD-PD with different horizon sizes δ are plotted together in Fig. 13 for two cross-section along $x = 0$ and $y = 0$.

It can be seen from Fig. 13 that with decreasing of the horizon size, the stress component σ_{xy} at the boundaries converge to zero for both paths, $x = 0$ and $y = 0$, which is consistent with the assumed traction-free boundary conditions. Near the dislocation core, all stress components increase abruptly. It should be pointed out that the stress components near the dislocation core computed by DC DDD-PD are significantly lower than those from the new SP DDD-PD scheme, or the SP DDD-FEM scheme. This shows the loss of accuracy present in the DC DDD-PD scheme when dislocations are too close.

4.1.2. Solution for a circular domain

Classical SP models can easily deal with straight boundaries (e.g., the square domain in the previous section). However, classical SP models have trouble when dealing with curved boundaries, since they needs to track the boundaries and their normals. In this sub-section, we consider a BVP with an edge dislocation in a cylinder ($R = 1.0$ μm, shown in Fig. 14). The stress field has been analytically

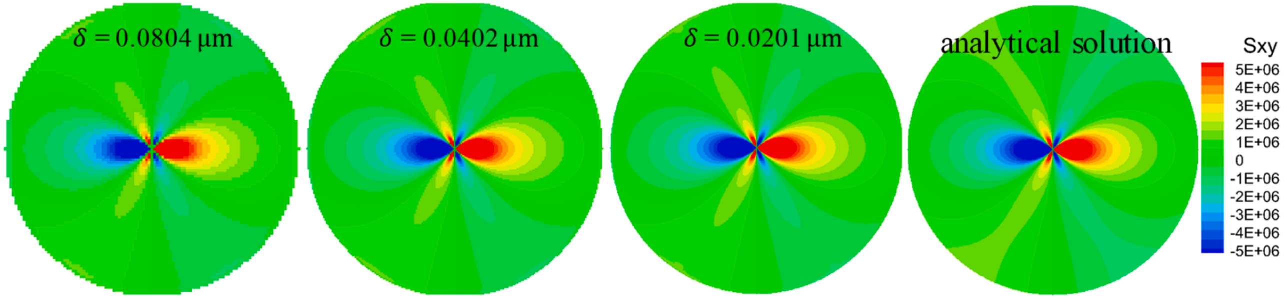

Fig. 15. Stresses σ_{xy} obtained by using the SP DDD-PD model, with different horizon sizes: $\delta = 0.0804$, 0.0402 and 0.0201 μm, and from the analytical solution for the cylinder case (Cai and Nix, 2016).

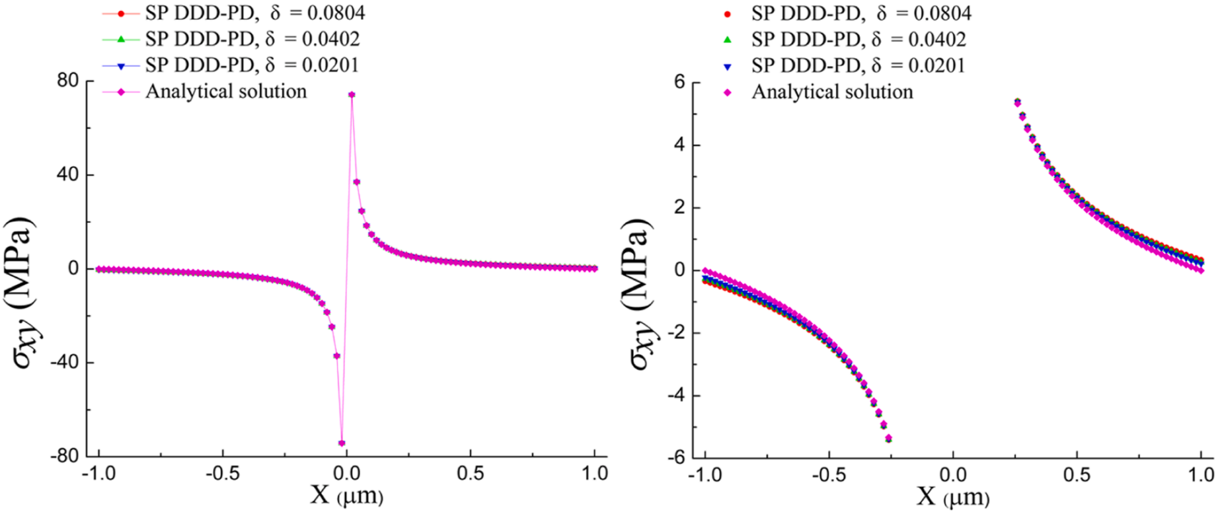

Fig. 16. Stress profiles from the SP DDD-PD model and the analytical solution for the cylinder with a slip plane problem: σ_{xy} on $y = 0$ μm. The left panel shows results over the full stress scale, while the right panel shows the same results but on a narrower stress range to more clearly observe the differences between the different solutions near the domain boundaries.

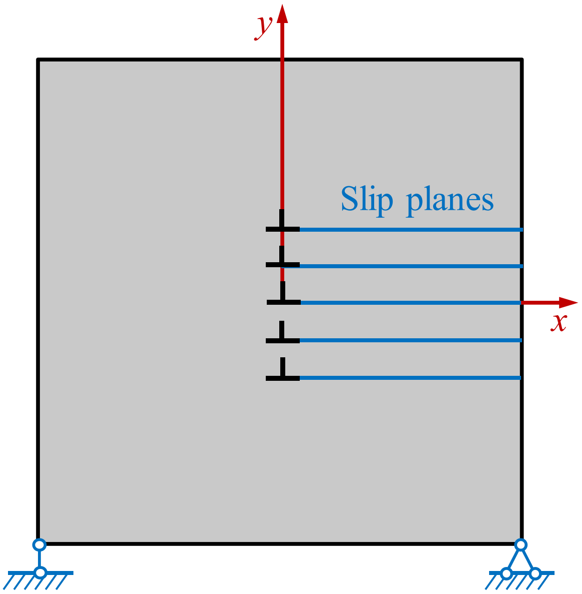

Fig. 17. Domain, dislocation positions, and boundary conditions for the multiple slip-planes problem.

solved for and shown in (Cai and Nix, 2016). The stress expressions are:

$$\begin{cases} \sigma_{rr} = -\dfrac{\mu b\sin\theta}{2\pi r(1-\nu)}\left[1-\left(\dfrac{r}{R}\right)^2\right] \\ \sigma_{\theta\theta} = -\dfrac{\mu b\sin\theta}{2\pi r(1-\nu)}\left[1-3\left(\dfrac{r}{R}\right)^2\right] \\ \sigma_{r\theta} = \dfrac{\mu b\cos\theta}{2\pi r(1-\nu)}\left[1-\left(\dfrac{r}{R}\right)^2\right] \end{cases} \tag{17}$$

For the SP DDD-PD model, the horizon factor m is fixed at 4.02. Different horizon sizes $\delta = 0.0804$, 0.0402 and 0.0201 μm are applied, corresponding to 9145, 33,947 and 130,721 nodes. Fig. 15 and Fig. 16 compare the results from the SP DDD-PD model with the analytical solution from (Cai and Nix, 2016), from which it can be concluded that the SP DDD-PD results converge to the analytical solutions.

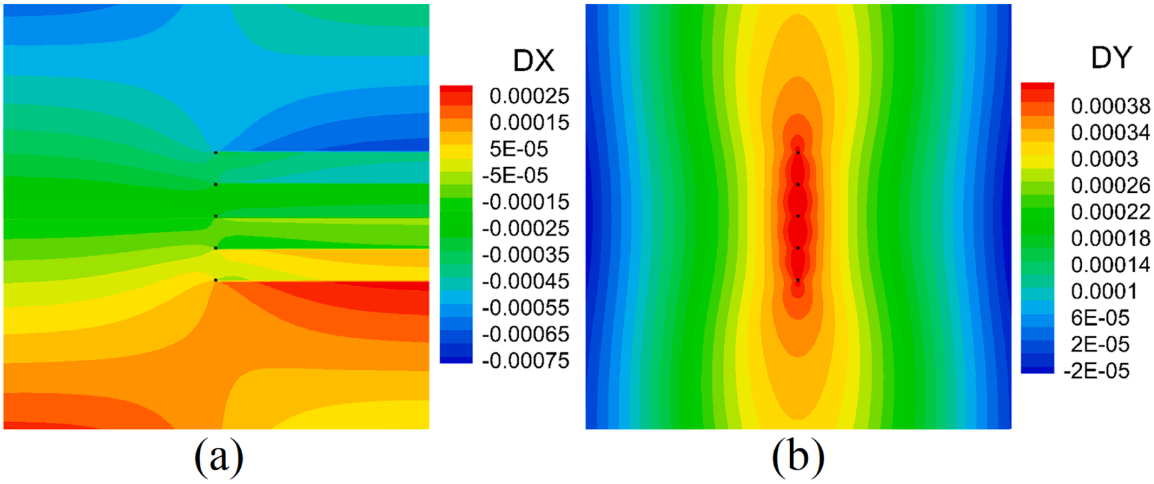

Fig. 18. (a) Horizontal and (b) vertical displacement fields obtained by using the SP DDD-PD model.

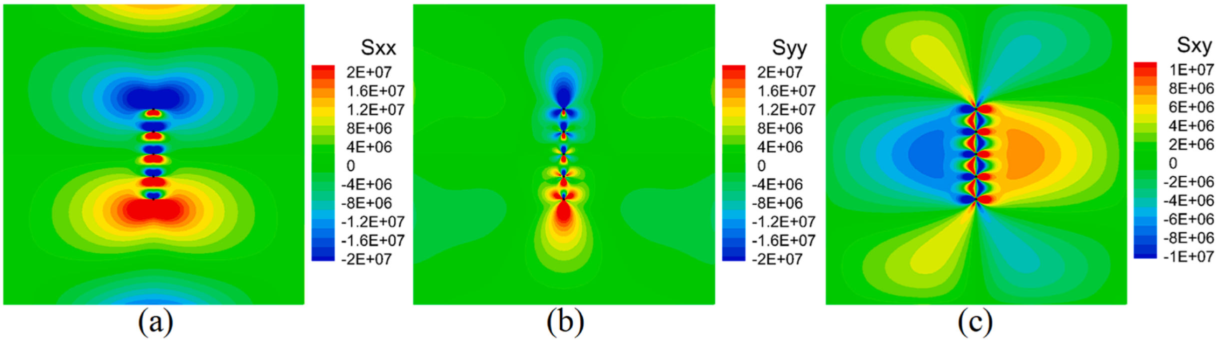

Fig. 19. Stresses (a) σ_{xx}; (b) σ_{yy}; (c) σ_{xy} obtained by using the SP DDD-PD model.

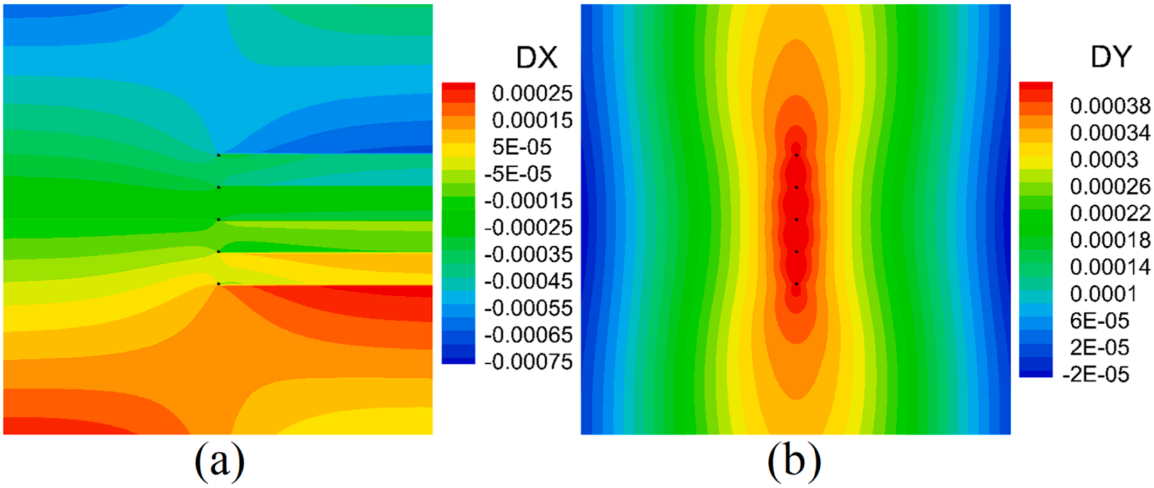

Fig. 20. (a) Horizontal and (b) vertical displacement fields obtained by using the SP DDD-FEM model.

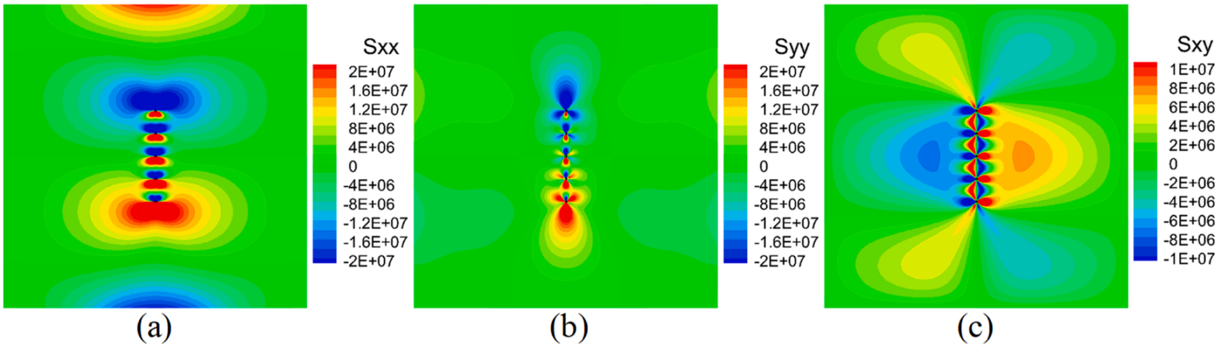

Fig. 21. Stresses (a) σ_{xx}; (b) σ_{yy}; (c) σ_{xy} obtained by using the SP DDD-FEM model.

4.2. *Interactions between multiple edge dislocations*

In this subsection, the model with a row of dislocations is simulated to verify the feasibility of the new SP DDD-PD scheme in dealing with interactions between adjacent dislocations. As shown in Fig. 17, the same setup as that used in the last subsection is applied, except that five dislocations on parallel slip planes, instead of one single edge dislocation, are embedded in the single crystal. We also compute the results using the SP DDD-FEM and the DC DDD-PD models. In the PD simulations (for both SP and DC schemes), the horizon factor m is set to 4.02, and the horizon size δ is set to 0.0402 μm.

The SP DDD-PD numerical results for displacement and stress fields are plotted in Fig. 18 and Fig. 19, respectively. The corresponding results by the SP DDD-FEM are provided in Fig. 20 and Fig. 21. Results from the two methods are close to each other.

To analyze the accuracy of stress results, we choose two cross-sections along $x = 0$ and $y = 0$. The stress components σ_{xx}, σ_{yy}, and σ_{xy} along these cross-sections computed by the three methods are plotted in Fig. 22. It reveals that the DC DDD-PD scheme grossly underestimates the stress magnitude near the dislocation cores. Therefore, it is difficult to simulate the interaction between neighboring dislocations by the DC DDD-PD scheme, while the SP DDD-PD scheme has no such limitations.

4.3. *Dislocation emitted from a crack tip*

It is well known that PD has a significant advantage in dealing with crack-related problems. For this, the SP DDD-PD scheme is developed and then applied to simulate dislocation-based elastoplastic fracture problems in Part II of this work (Dong et al., al.). In this subsection, the stress field by an edge dislocation emitted from a crack tip is calculated by the present SP DDD-PD scheme. The computed stress contours are compared with the results reported in the literature to further validate the applicability of the new SP DDD-PD scheme for problems with cracks.

The geometry and boundary conditions are shown in Fig. 23, where a square single crystal with side length $L = 4$ μm is simply-supported on the bottom side. A horizontal edge crack is inserted on the left side of the crystal, with the crack tip located at the model center. An edge dislocation emitted from the crack tip is introduced on the inclined slip plane. The intersection angle between the dislocation slip plane and the crack tip surface is 60° Material parameters and PD parameters (i.e., horizon size and horizon factor) are selected as the same as those used in the previous subsection.

The same problem has been simulated by the DDD-XFEM model in (Liang et al., 2019). Only the normal stress component σ_{yy} was presented there. This component is obtained by our new SP DDD-PD model and plotted in Fig. 24, using the same contour scale bar as in (Liang et al., 2019). Our result agrees well with both (Liang et al., 2019) and the theoretical result by (Farkas et al., 2001). The shielding effect on the crack tip by the emitted dislocation is accurately captured. We conclude that the new SP DDD-PD scheme is a reliable framework for studying quasi-static plastic fracture problems with both cracks and dislocations. The advantage of the SP DDD-PD scheme in problems with cracks, versus classical methods like DDD-FEM, DDD-XFEM, is its ability to simulate unrestricted evolution of crack/damage growth, and now dislocations. This will be further provided in Part II of this work (Dong et al., al.).

4.4. *Interaction between a dislocation and a void*

To further validate the SP DDD-PD scheme, the case for interaction between an edge dislocation and a cylindrical void is considered in this subsection, since ductile fracture of metallic materials is usually accompanied by nucleation, growth, and coalescence of/from microvoids. Therefore, it is crucial to understand the interaction between dislocations and microvoids in ductile materials.

Within the SP DDD-PD framework, voids with any shapes can be considered easily. Since the analytical solution for an edge dislocation near a cylindrical void can be readily found (Dundurs and Mura, 1964), only the cylindrical void is taken into account to validate the present SP DDD-PD scheme. The schematic of the void-dislocation interaction model is shown in Fig. 25. The Airy stress function for this problem is (Dundurs and Mura, 1964):

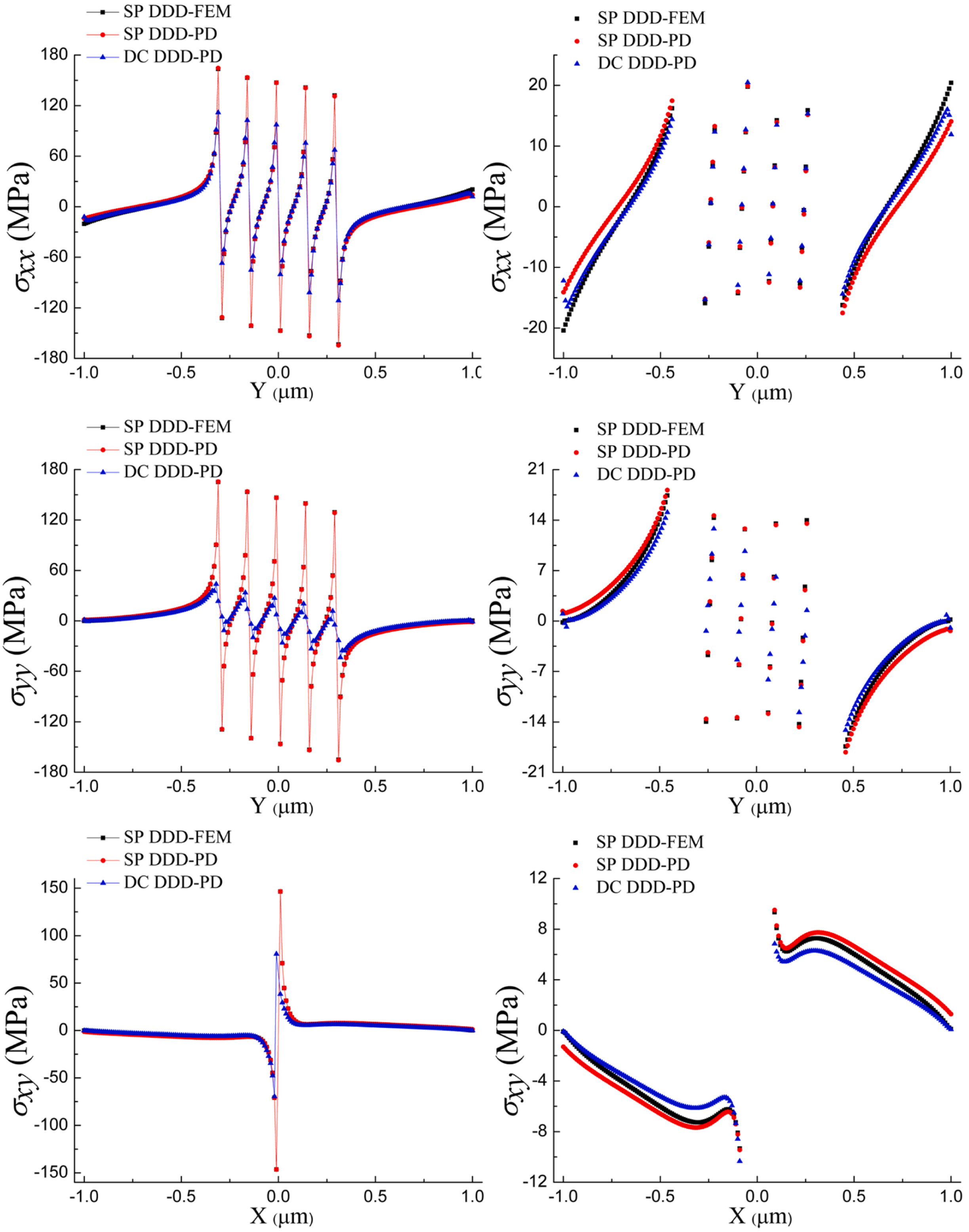

Fig. 22. Stress profiles from three DDD models (SP DDD-FEM, SP DDD-PD, and DC DDD-PD): σ_{xx} on $x = 0$ μm (top panels), σ_{yy} on $x = 0$ μm (middle panels) and σ_{xy} on $y = 0$ μm (bottom panels). The left panels show results over the full stress scale, while the right panels show the same results but on a narrower stress range to more clearly observe the differences between the different solutions near the domain boundaries.

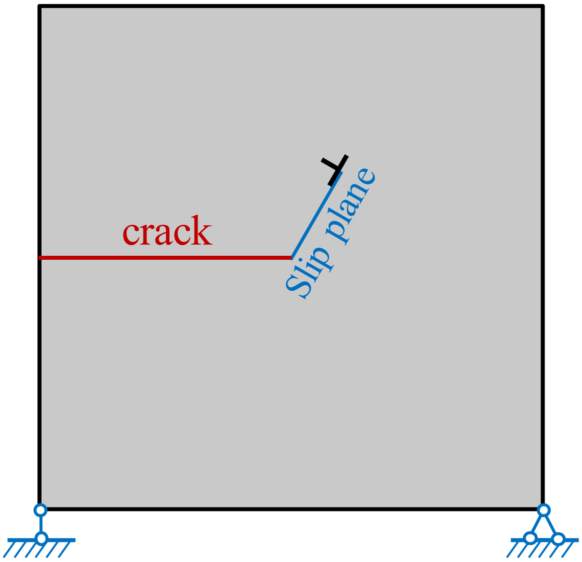

Fig. 23. Geometry and boundary conditions for an edge dislocation emitted from a crack tip.

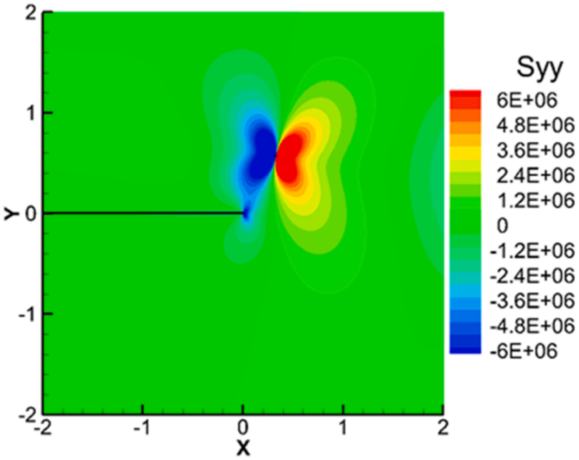

Fig. 24. Stress contours (σ_{yy}) obtained by the SP scheme of the DDD-PD model.

$$\phi(r,\theta)=\frac{Gb}{\pi(k+1)}\left\{-2r_1\ln r_1\sin\theta_1+2(r_2\ln r_2\sin\theta_2-r\ln r\sin\theta)-R\left(\frac{1}{\beta}-\frac{1}{\beta^3}\right)\left[\sin2\theta_2-R\left(\beta-\frac{1}{\beta}\right)\frac{\sin\theta_2}{r_2}\right]-R^2\frac{\sin\theta}{r}\right\} \tag{18}$$

where R is the radius of the void, r, r_1 are the distances from the considered material point to the void center and the dislocation core, respectively. r_2 is the distance from the considered material point to the image point of the dislocation core inside the void. The image point is located at the position of $(r^*, 0)$, where $r^* = \frac{R^2}{r'}$. As shown in Fig. 25, r' is the distance between the dislocation core and the void center. Other geometrical parameters, such as θ, θ_1, and θ_2, are illustrated in Fig. 25. By the Airy stress function given in Eq. (18), the stress components at any point induced by the dislocation can be obtained easily (Dundurs and Mura, 1964).

Three different cases are considered in the dislocation-void interaction model, as shown in Fig. 26. The side length of the model L and the distance between dislocation and void center r' are selected as $\{L = 2.6\ \mu\text{m}, r' = 0.4\ \mu\text{m}\}$, $\{L = 2.6\ \mu\text{m}, r' = 0.25\ \mu\text{m}\}$ and $\{L = 4.0\ \mu\text{m}, r' = 0.25\ \mu\text{m}\}$ for Case 1, Case 2 and Case 3, respectively. The void radius R is fixed as 0.15 μm. The material parameters are the same as those in the above three simulation models. The horizon factor and the horizon size δ are selected as 4.02 and 0.0201μm. The smaller horizon size used in this example, compared to the earlier ones, is due to the consideration of the void size. A dislocation slip towards the void is considered.

In Fig. 27, the shear stress fields for this problem by the theoretical formula (Dundurs and Mura, 1964), the present SP DDD-PD scheme and the DC DDD-PD scheme are shown. It should be pointed out that the analytical solution by Eq. (18) is not used in the present SP DDD-PD scheme. Instead, only the simple analytical field for dislocation embedded in the infinite body is employed here by

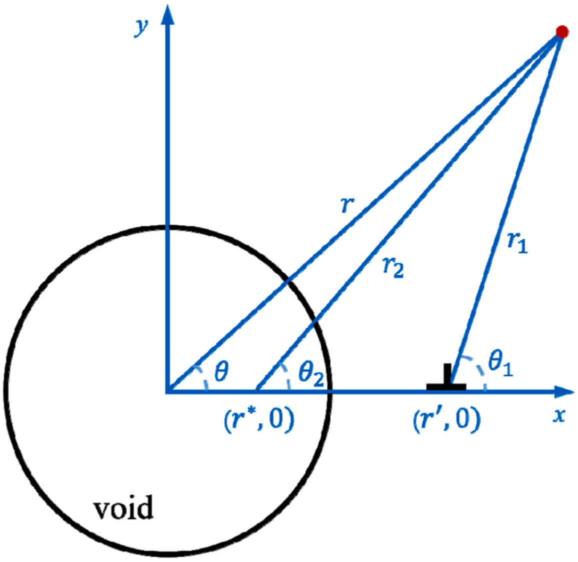

Fig. 25. The schematic of void-dislocation coordinates system.

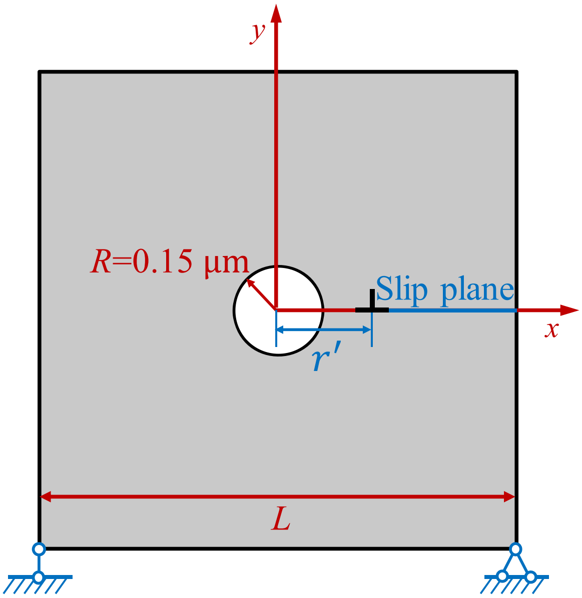

Fig. 26. Void-dislocation setup and boundary conditions.

Eq. (12). In the PD models, a uniform grid is adopted here, for simplicity, to discretize the crystal, although a non-uniform grid conforming to the void boundary would increase the computational accuracy. The application of a non-uniform grid in the SP DDD-PD scheme will be performed in the future. The result obtained by the present SP DDD-PD scheme agrees well with the theoretical solution, while the results from the DC DDD-PD scheme clearly indicate a significant loss of accuracy the closer the dislocation is to the void. This means that the DC DDD-PD scheme cannot capture dislocation-void interaction accurately. This is why some additional techniques are needed when using the DC scheme to simulate the interactions between dislocations and neighboring voids (or other types of defects).

To further analyze the accuracy of the DDD-PD schemes for solving the dislocation-void interaction problem, the results of the shear stress component σ_{xy} are plotted along the $y = 0$ μm cross-section in Fig. 28. The result by the present SP DDD-PD scheme matches better with the analytical solution by (Dundurs and Mura, 1964) than that by the DC DDD-PD scheme, especially near the dislocation core (see the right panel of Fig. 28). When the dislocation density is high (i.e., the dislocations are close enough) or when the distance between dislocations and different kinds of defects is small enough, the present SP DDD-PD scheme is more suitable than the DC DDD-PD scheme. Note that the analytical solution by (Dundurs and Mura, 1964) is for the problem in an infinite domain, while the problem shown in Fig. 26 is over a finite domain. Therefore, the comparison is not strictly valid, especially for locations near the

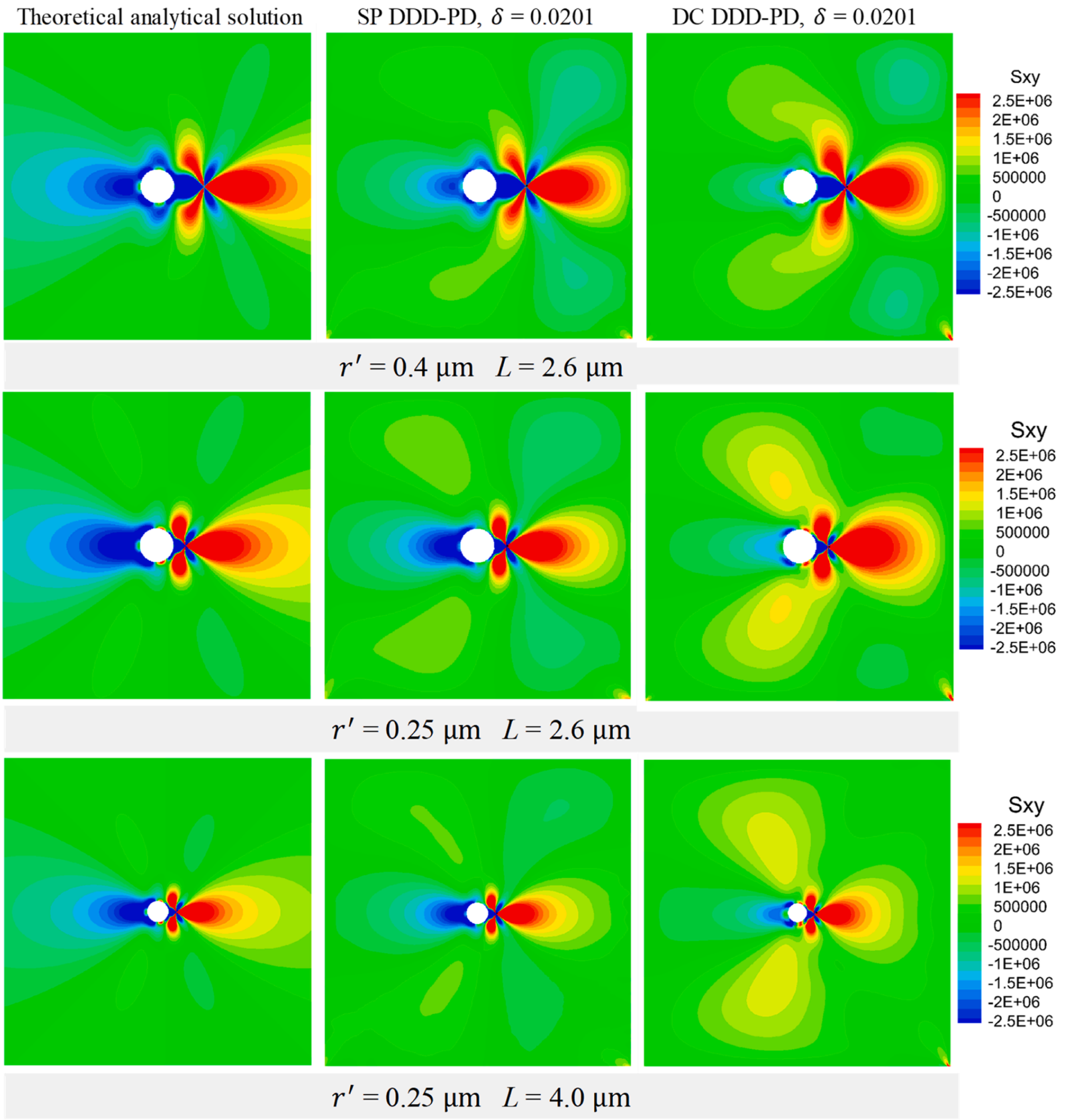

Fig. 27. The distributions of shear stresses obtained from the PD models and the analytical solution.

boundary of the finite domain.

Computational efficiency is a big concern for the model and computation method to be applied for simulating or predicting physical and chemical processes. The computation efficiency of peridynamic model is usually lower than the classical PDE-based methods. To apply the SP DDD-PD model for the 3D cases, one needs to solve the computational efficiency issue. Coupling PD with the local models, such as FEM, to obtain a numerical model with the advantages of two computational techniques provides a method to deal with this issue (see (Galvanetto et al., 2016; Pagani and Carrera, 2020)). Another promising way is a convolution-based method, which can reduce the computational complexity of PD models from $O(N^2)$ to $O(N\log_2 N)$, with N being the total number of discretization nodes (see (Jafarzadeh et al., 2020, 2022)).

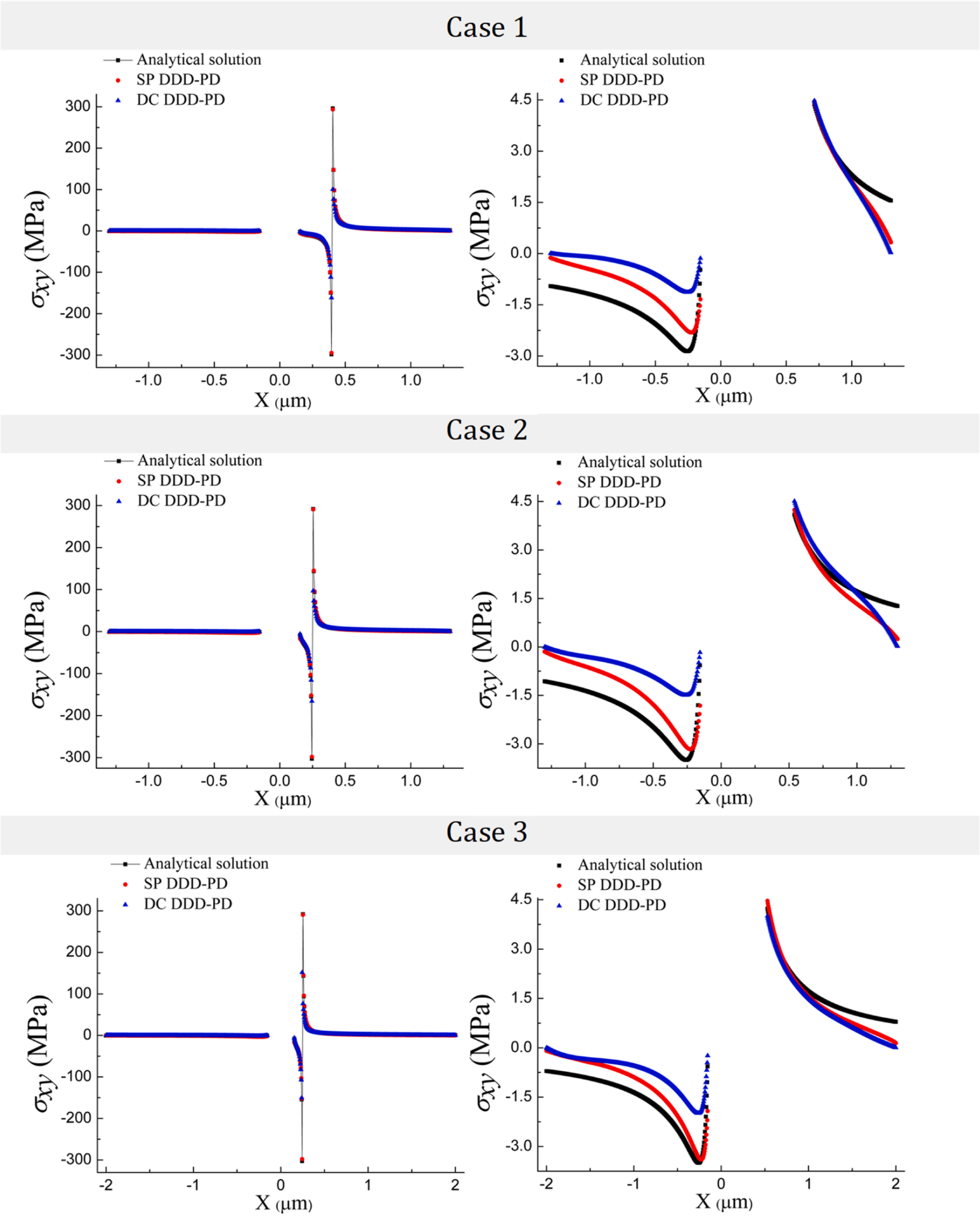

Fig. 28. σ_{xy} profiles on line $y = 0$ μm for all three cases, obtained from the PD models and the analytical solution for the interaction between a void and a dislocation. The left panels show results over the full stress scale, while the right panels show the same results but on a narrower stress range to more clearly observe the differences between the different solutions near the domain boundaries.

5. Conclusions

A peridynamic (PD) approach, based on the superposition (SP) scheme, is introduced here to solve discrete dislocation dynamics (DDD) problems. The key difference between the classical SP scheme and the SP DDD-PD scheme introduced in this work is the replacement of the local model in the complementary problem with a nonlocal/peridynamic one. This replacement eliminates the need for explicitly tracking boundaries, interfaces, cracks, etc. in the classical models, and makes the PD model very general and flexible. In this way, traction boundaries on arbitrary domains, cracks, damaged regions, and voids are treated in a unified way.

The new SP DDD-PD scheme is verified by solving several BVPs for single dislocation, multiple dislocations, dislocation emitted from the crack tip, and dislocation-void interaction. The simulation results from the new method are compared with theoretical solutions and with those calculated by the discrete-continuous (DC) DDD-PD, SP DDD-FEM, and DDD-XFEM schemes. The results by the present SP DDD-PD scheme agree well with the theoretical solutions even near the dislocation core. The results for dislocation-dislocation, dislocation-crack and dislocation-void interactions are also accurately computed by the SP DDD-PD scheme. We noted that the DC DDD-PD scheme significantly underestimates the interactions between dislocations, between dislocation and crack, and between dislocation and void when they are close enough. Some additional complex techniques are required for the DC DDD-PD scheme to simulate the dislocation evolution, while these are not needed for the new SP DDD-PD scheme.

In Part II of this work (Dong et al., al.), the SP DDD-PD scheme is further employed to consider nucleation, glide, annihilation, and other evolution of dislocations. Further, it is applied to simulate elastoplastic deformation and fracture of crystalline materials, showing a significant advantage over other schemes in dealing with such complex problems.

Declaration of Competing Interest

The authors declare that they have no known competing financial interests or personal relationships that could have appeared to influence the work reported in this paper.

Data Availability

No data was used for the research described in the article.

Acknowledgements

This work was supported by the Natural Science Foundation of China (No. 11802098, No. 11822204) and the Fundamental Research Funds for the Central Universities (No. 2021GCRC021). The work of F.B was supported in part by the National Science Foundation under CMMI CDS&E award No. 1953346. The authors would like to thank the anonymous reviewers for constructive comments and suggestions that have led to significant improvements.

Appendix A. Surface correction methods for peridynamic modeling

Surface correction methods for PD can be divided into two categories (Le and Bobaru, 2018): methods in the first category modify either the bond stiffness for bonds near the surface to have a better match between PD and classical mechanics for homogeneous deformations, using different criteria (based on the interaction volume, the force density, or energy density). All correction methods show some improvement for the displacement profile when compared with the uncorrected bond-based formulations. The PD surface effect, however, is, only reduced, not eliminated, in general. Methods in the second category attempt to “restore” the missing bonds for PD nodes near the surface so that each material point “feels” like a material point in the bulk; this is used by the fictitious nodes method (FNM). The FNM is used in the present work also for enforcing local Dirichlet and Neumann BCs.

The FNM employs fictitious nodes around the domain boundary so that every real material point has a full neighborhood. To do so, the layer of fictitious nodes must be of thickness at least equal to one-horizon size around the original domain. This method eliminates any need to modify the PD formulation, thus it is directly applicable to all PD models. The method does not apply explicit external constraints on real PD nodes, instead it applies displacement constraints on fictitious nodes. The forces fictitious nodes act on the real nodes can create the desired local-type boundary conditions. The mirror-based FNM or simply “mirror FNM” assigns the constraint at each fictitious point based on the current solution of its mirror point in the domain. Two points are a pair of mirror points if they are “symmetric” to the boundary. In this method, one assumes that for each fictitious point $\boldsymbol{x}_\Gamma$, its mirror point $\boldsymbol{x}_\Gamma^m$ is given as shown in Fig. 29 where $\boldsymbol{x}_\Gamma^b$ is the mid-point of $\overrightarrow{\boldsymbol{x}_\Gamma \boldsymbol{x}_\Gamma^m}$ sitting on the boundary. When the boundary is smooth in a neighborhood (of size that depends on geometry) of $\boldsymbol{x}_\Gamma^b$, $\overrightarrow{\boldsymbol{x}_\Gamma \boldsymbol{x}_\Gamma^m}$ is collinear with the normal vector $\boldsymbol{n}_b$ to the boundary at $\boldsymbol{x}_\Gamma^b$.

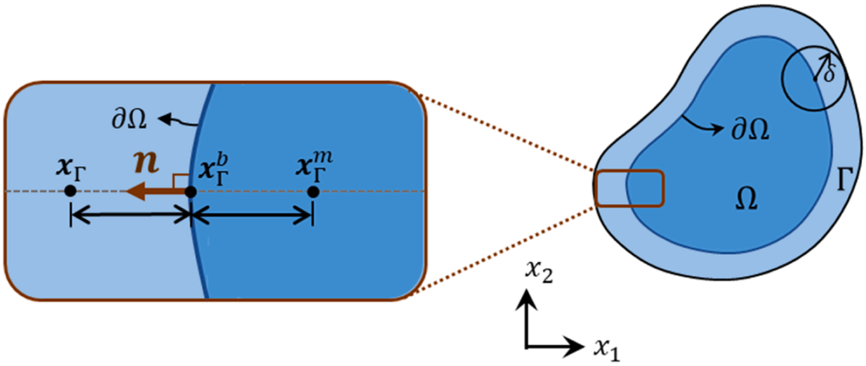

Fig. 29. Fictitious nodes method for imposing local BCs on ∂Ω by assigning certain constraints at fictitious points in Γ based on current values at their mirror points, inside Ω, and the value of the boundary condition to be imposed (Zhao et al., 2020).

To enforce the local Dirichlet BC $\boldsymbol{u}(\boldsymbol{x},t) = \boldsymbol{u}_\mathrm{D}(\boldsymbol{x})$ for $\boldsymbol{x} \in \partial\Omega_\mathrm{D}$ for $\boldsymbol{x} \in \partial\Omega_\mathrm{N}$ in the mirror FNM, the constraint at a generic fictitious point $\boldsymbol{x}_\Gamma$ is written as:

$$\boldsymbol{u}_\Gamma = 2\boldsymbol{u}_\Gamma^b - \boldsymbol{u}_\Gamma^m \tag{A1}$$

where $\boldsymbol{u}_\Gamma = \boldsymbol{u}(\boldsymbol{x}_\Gamma,t)$, $\boldsymbol{u}_\Gamma^b = \boldsymbol{u}(\boldsymbol{x}_\Gamma^b,t)$, $\boldsymbol{u}_\Gamma^m = \boldsymbol{u}(\boldsymbol{x}_\Gamma^m,t)$, and $\overrightarrow{\boldsymbol{x}_\Gamma\boldsymbol{x}_\Gamma^b} = \overrightarrow{\boldsymbol{x}_\Gamma^b\boldsymbol{x}_m}$ is the distance between $\boldsymbol{x}_\Gamma$ and $\boldsymbol{x}_\Gamma^m$. The mirror FNM is exact in 1D and reasonably accurate in 2D and 3D where the body shape is simple and the unknown function variation, in a δ region near the boundary, is close to linear (e.g. homogeneous deformations).

The mirror FNM eliminates the PD surface effect for homogeneous deformations on domains with simple geometries. However, for the general case, to find mirror pairs one needs to find the distance between each point and the boundary, and, for each fictitious point, find the corresponding mirror point in the domain. While providing such information is simple and straightforward for simple geometries, it is not so for arbitrary ones, for example shapes with sharp corners, cusps and crack tips, etc. At such locations, the tangent line (and normal vector) may not be well defined. While some ad-hoc choices can be made for overcoming this issue, (Zhao et al., 2020) proposed a general algorithm that generates a well-defined "generalized" normal vector to the boundary at any of its points, regular or not, so that both the mirror point and the distance from the point to the boundary can be determined without ambiguity.

Appendix B. Discretization

One-point Gaussian quadrature (Silling and Askari, 2005), modified with the partial-volume algorithm mentioned below, is employed for approximating the integral in the equilibrium equations. Uniform grids are adopted to discretize the PD models, with grid spacing denoted by Δx. Non-uniform grids are possible in discretizing the PD equations (see (Bobaru and Ha, 2011; Henke and Shanbhag, 2014; Li et al., 2018)) but this is not pursued here. For each node, its family is constructed within the horizon, as a pre-processing step. The discrete version of Eq. (1) at a given node $\boldsymbol{i}$ with coordinate $\boldsymbol{x}_i$ is (Littlewood, 2015):

$$\sum_{j \epsilon H_i} \boldsymbol{f}\left(\boldsymbol{x}_j - \boldsymbol{x}_i, \boldsymbol{u}_j - \boldsymbol{u}_i\right)\Delta A_j = 0 \tag{A2}$$

where $\boldsymbol{x}_j$ is the coordinate of the node j inside the horizon region of node i. ΔA_j is the nodal area (volume in 3D) of node j covered by the horizon of node i. For the estimation of nodal volumes which are only partially covered by the horizon of node i, several algorithms have been proposed (Bobaru and Ha, 2011; Seleson and Littlewood, 2016). The HHB algorithm by (Bobaru and Ha, 2011) is used in this work. It has been shown that this particular approximation is very close to the exact algorithm discussed in (Seleson and Littlewood, 2016), and has the advantage of simplicity and efficiency.

The nonlinear conjugate gradient (NCG) method is used to solve the nonlinear (in displacements) system described by Eq. (A2). This is similar to the algorithm used in (Xu et al., 2018) and (Zhang and Bobaru, 2016), except that the stopping criterion presented in (Shewchuk, 1994) with a more efficient hybrid conjugate gradient (CG) algorithm (Dai and Yuan, 2001) is employed to find β. The complete CG method is available in (Shewchuk, 1994).

In the computations, it is necessary to differentiate between bonds crossing a dislocation slips and those not crossing slip planes. Consider that the coordinates of two slip ends are $\boldsymbol{A} = (x_1,y_2)$, $\boldsymbol{B} = (x_2,y_2)$ and a PD bond has two ends $\boldsymbol{C} = (x_3,y_3)$, $\boldsymbol{D} = (x_4,y_4)$. Then the line segments can be expressed as $\boldsymbol{AB} = \boldsymbol{p} + t\boldsymbol{r}$ and $\boldsymbol{CD} = \boldsymbol{q} + u\boldsymbol{s}$, where $\boldsymbol{p} = \boldsymbol{A}$, $\boldsymbol{r} = \boldsymbol{B} - \boldsymbol{A}$, $\boldsymbol{q} = \boldsymbol{C}$, $\boldsymbol{s} = \boldsymbol{D} - \boldsymbol{C}$, and $\{t = \frac{(\boldsymbol{p}-\boldsymbol{q})\times \boldsymbol{s}}{\boldsymbol{r}\times \boldsymbol{s}}, u = \frac{(\boldsymbol{q}-\boldsymbol{p})\times \boldsymbol{r}}{\boldsymbol{r}\times \boldsymbol{s}}\}$. The algorithm used to judge whether a bond is crossed by any slip plane or not is shown in Fig. 30.

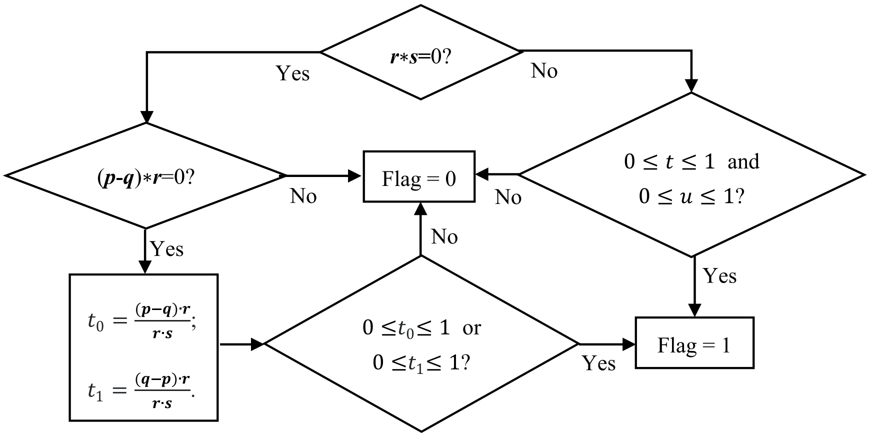

Fig. 30. Algorithm for judging whether a bond is crossing any slip plane. Flag = 1 means crossing.

Appendix C. Calculation of stress components in 2D bond-based peridynamics

In this appendix we provide the algorithms to compute the stress tensor based on the deformation and the PD force (Algorithm 1), and to evaluate the stress components in the local coordinate system aligned with a particular slip plane, that makes an angle \theta with the x-coordinate direction (Algorithm 2).

Algorithm 1: Stress calculation of 2D bond-based PD code at node x_i

```
$\boldsymbol{\sigma}_i = 0$                                   ! Stress tensor at node $\boldsymbol{x}_i$
For all nodes $\boldsymbol{x}_j \in H_{\boldsymbol{x}_i}$
$\boldsymbol{\xi} = \boldsymbol{x}_j - \boldsymbol{x}_i$
$\boldsymbol{\eta} = \boldsymbol{u}_j - \boldsymbol{u}_i$
$s = \frac{\| \boldsymbol{\eta} + \boldsymbol{\xi} \| - \| \boldsymbol{\xi} \|}{\| \boldsymbol{\xi} \|}$
$c = \frac{48E}{5\pi\delta^3}$
$f = \frac{\boldsymbol{\xi} + \boldsymbol{\eta}}{\| \boldsymbol{\xi} + \boldsymbol{\eta} \|} csV_j$
$\boldsymbol{\sigma}_i = \boldsymbol{\sigma}_i + \frac{1}{2}\boldsymbol{f} \otimes \boldsymbol{\xi}$
End of loop for nodes $\boldsymbol{x}_j \in H_{\boldsymbol{x}_i}$
```

Algorithm 2: stress components in the local coordinate system, defined by a slip plane, at node x_i

```
$\sigma_{xx} = [\boldsymbol{\sigma}_i]_{11};\ \sigma_{yy} = [\boldsymbol{\sigma}_i]_{22}; \sigma_{xy} = [\boldsymbol{\sigma}_i]_{12}$          ! Stress components at node $(x_i, y_i)$
For all dislocations $(x_j, y_j)$
$x_{ij} = x_i - x_j; y_{ij} = y_i - y_j$
$x' = x_{ij}\cos\theta + y_{ij}\sin\theta; y' = -x_{ij}\sin\theta + y_{ij}\cos\theta$          ! Local coordinates; \theta is the angle of the slip plane with the x-coordinate direction
$D = \frac{\mu b}{2\pi(1-\nu)}$
$\sigma'_{xx} = -\frac{Dy'(3x'^2 + y'^2)}{(x'^2 + y'^2)^2}; \sigma'_{yy} = \frac{Dy'(x'^2 - y'^2)}{(x'^2 + y'^2)^2}; \sigma'_{xy} = \frac{Dx'(x'^2 - y'^2)}{(x'^2 + y'^2)^2}$
! Stress components in the local coordinates
$\sigma_{xx} = \sigma_{xx} + \sigma'_{xx}\cos^2\theta + \sigma'_{yy}\sin^2\theta - \sigma'_{xy}\sin2\theta;$
$\sigma_{yy} = \sigma_{yy} + \sigma'_{xx}\sin^2\theta + \sigma'_{yy}\cos^2\theta + \sigma'_{xy}\sin2\theta;$
$\sigma_{xy} = \sigma_{xy} + \frac{1}{2}(\sigma'_{xx} - \sigma'_{yy})\sin2\theta + \sigma'_{xy}\cos2\theta$          ! Global coordinates
End of loop for dislocations $(x_j, y_j)$
```

Appendix D. Non-zero net PD force near the dislocation core, introduced by the numerical approximation

In this appendix, the non-zero net PD force near the dislocation core that is introduced by the numerical approximation is discussed. In the numerical method of PD, the computational domain is discretized into a set of cells (volumes, areas, segments) that have the discretization nodes at their centers, essentially the one-point Gaussian integration method modified as discussed in Appendix B. As with any numerical discretization, errors are introduced, especially in areas with high gradients. To reduce these errors, a fine grid helps, but this leads to lower computational efficiency, and a balance between these two requirements has to be found. To improve the computational efficiency, the relative mesh size m cannot be too large, and in this paper, we select $m = 4.02$. Although a recently-introduced fast convolution-based method for peridynamics leads to more efficient calculations and thus calculations with large m values are possible (Jafarzadeh et al., 2022, 2021), more effort is needed to make this method suitable for problems studied here. Near the dislocation core, stress gradients blow up, and the error in calculating the resultant PD bond force at nodes near it, introduced by the one-point Gaussian integration method with a small m value, can be large. Because of this, instead of the analytical zero PD force (from equilibrium), we compute a relatively high non-zero net bond force at nodes near the core. Obviously, this happens in any numerical approximation of the classical model as well, as seen from the example below.

To show the effect of m value, a typical point with coordinate $(0.6\ \mu\text{m}, 0.8\ \mu\text{m})$ relative to the origin (i.e., the edge dislocation core in Fig. 4) is considered. The resultant PD force at this point is plotted in Fig. 31 for different $m = 3.0,\ 3.1,\ 3.2,\ \ldots,\ 20.0$ and fixed $\delta = 0.08\ \mu\text{m}$. The resultant net PD force components along both x and y directions are provided. It can be clearly seen from Fig. 31 that the resultant net PD force converges to zero, but the convergence is not monotonic.

This non-zero net force is also found in numerical approximations of the classical model. For example, using the finite difference method (FDM), a similar behavior is found. To exemplify this, we recall the classical equilibrium equation expressed in displacements:

$$(\lambda + G)\nabla\nabla \cdot \boldsymbol{U} + G\ \nabla \cdot \nabla \boldsymbol{U} + \boldsymbol{F} = 0 \tag{A3}$$

where λ and G are the Lamé constants, $\boldsymbol{U}$ is the displacement and $\boldsymbol{F}$ is the body force (which is 0 in this problem). Using the central difference scheme to discretize the left-hand side, and setting $\Delta x_1 = \Delta x_2 = \Delta s$, the first component of the remainder of this equation thus becomes

$$\begin{aligned}\widetilde{F}_x^{\mathrm{e}} = {} & \frac{(\lambda + G)}{4\Delta s^2}\left(4U_x^{(i+1,j)} + 4U_x^{(i-1,j)} - 8U_x^{(i,j)} + U_y^{(i+1,j+1)} + U_y^{(i-1,j-1)} - U_y^{(i+1,j-1)} - U_y^{(i-1,j+1)}\right) \\ & + \frac{G}{\Delta s^2}\left(U_x^{(i+1,j)} + U_x^{(i-1,j)} + U_x^{(i,j+1)} + U_x^{(i,j-1)} - 4U_x^{(i,j)}\right)\end{aligned} \tag{A4}$$

where the superscripts for U denote the indices discretization points in the two different directions, and the subscripts stand for the horizontal and vertical components. Then, the net force at the same material point $(0.6\ \mu\text{m}, 0.8\ \mu\text{m})$ is plotted in Fig. 32 for different relative mesh sizes $\delta/\Delta s = 3.0,\ 3.1,\ 3.2,\ \ldots,\ 20.0$ and fixed $\delta = 0.08\ \mu\text{m}$. The results in Fig. 32 show a monotonic convergence to zero net force as the grid density goes to infinity.

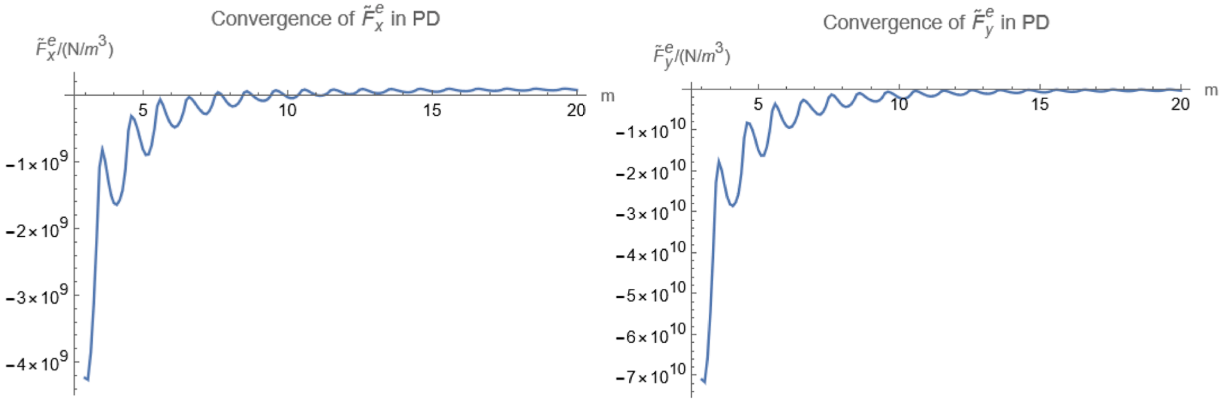

Fig. 31. Resultant PD force at a material point $(0.6\ \mu\text{m}, 0.8\ \mu\text{m})$ versus the horizon factor.

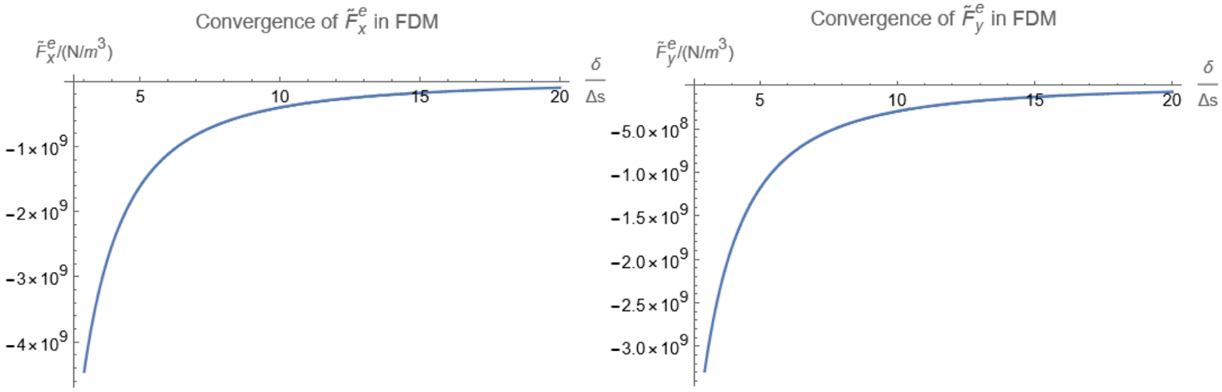

Fig. 32. Net force at a material point $(0.6\ \mu\text{m}, 0.8\ \mu\text{m})$ versus the horizon factor.

Appendix E

Displacement (Fig. 33) and stress fields (Fig. 34) calculated by the SP DDD-FEM model for the problem shown in Fig. 10

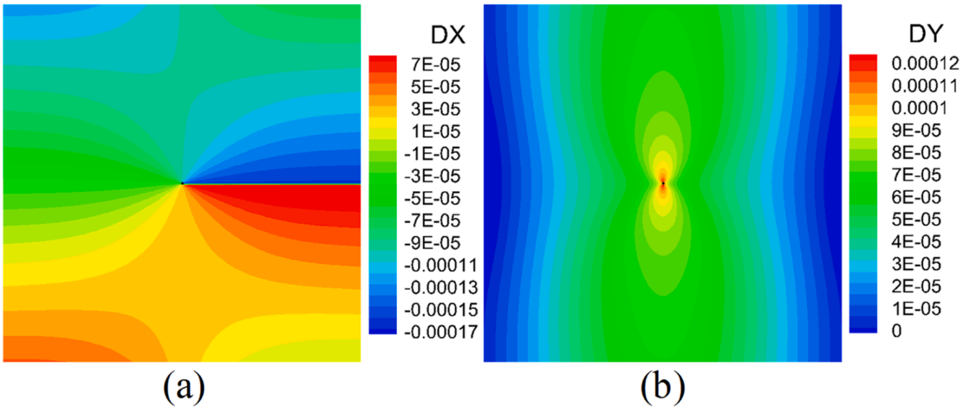

(a) (b)

Fig. 33. (a) Horizontal and (b) vertical displacements obtained by using the SP DDD-FEM model.

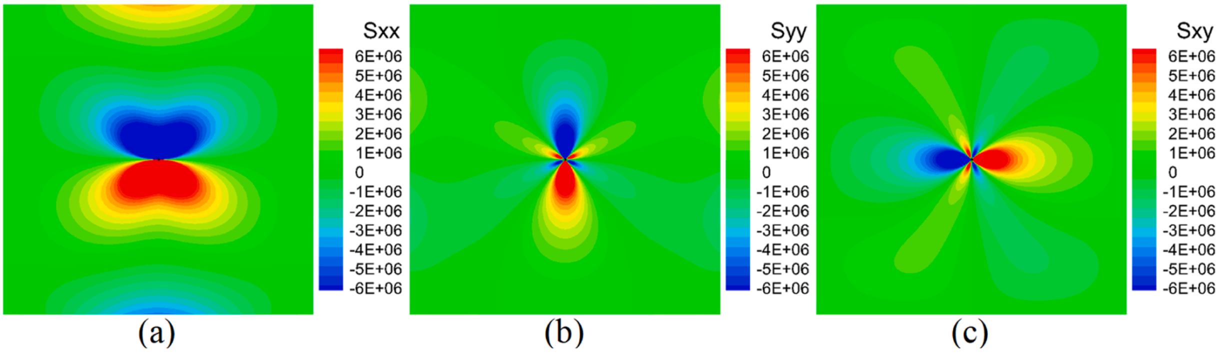

(a) (b) (c)

Fig. 34. Stresses (a) σ_{xx}, (b) σ_{yy}, and (c) σ_{xy} obtained by using the SP DDD-FEM model.

References

Anderson, P.M., Hirth, J.P., Lothe, J., 2017. Theory of Dislocations. Cambridge University Press.

Bobaru, F., Foster, J.T., Geubelle, P.H., Silling, S.A., 2016. Handbook of Peridynamic Modeling. CRC press.

Bobaru, F., Ha, Y.D., 2011. Adaptive refinement and multiscale modeling in 2D peridynamics. Int. J. Multiscale Comput. Eng. 9, 635–659.

Bobaru, F., Hu, W., 2012. The meaning, selection, and use of the peridynamic horizon and its relation to crack branching in brittle materials. Int. J. Fract. 176, 215–222.

Bobaru, F., Yang, M., Alves, L.F., Silling, S.A., Askari, E., Xu, J., 2009. Convergence, adaptive refinement, and scaling in 1D peridynamics. Int. J. Numer. Methods Eng. 77, 852–877.

Cai, W., Nix, W.D., 2016. Imperfections in Crystalline Solids. Cambridge University Press.

Chatterjee, S., Li, Y., Po, G., 2021. A discrete dislocation dynamics study of precipitate bypass mechanisms in nickel-based superalloys. Int. J. Plast. 145, 103062.

Chen, Z., Bakenhus, D., Bobaru, F., 2016. A constructive peridynamic kernel for elasticity. Comput. Methods Appl. Mech. Eng. 311, 356–373.

Chen, Z., Bobaru, F., 2015. Peridynamic modeling of pitting corrosion damage. J. Mechan. Phys. Solids 78, 352–381.

Chen, Z., Jafarzadeh, S., Zhao, J., Bobaru, F., 2021. A coupled mechano-chemical peridynamic model for pit-to-crack transition in stress-corrosion cracking. J. Mechan. Phys. Solids 146, 104203.

Chen, Z., Peng, X., Jafarzadeh, S., Bobaru, F., Analytical solutions of peridynamic equations. Part II: elastic wave propagation. Submitted.

Chen, Z., Peng, X., Jafarzadeh, S., Bobaru, F., 2022. Analytical solutions of peridynamic equations. Part I: transient heat diffusion. J. Peridyn. Nonlocal Model. 1–33.

Cheng, Z., Zhang, G., Wang, Y., Bobaru, F., 2015. A peridynamic model for dynamic fracture in functionally graded materials. Compos. Struct. 133, 529–546.

Cleveringa, H., Van der Giessen, E., Needleman, A., 2000. A discrete dislocation analysis of mode I crack growth. J. Mechan. Phys. Solids 48, 1133–1157.

Cleveringa, H., Van der Giessen, E., Needleman, A., 2001. A discrete dislocation analysis of rate effects on mode I crack growth. Mater. Sci. Eng.: A 317, 37–43.

Connolly, M., Martin, M., Bradley, P., Lauria, D., Slifka, A., Amaro, R., Looney, C., Park, J.-.S., 2019. In situ high energy X-ray diffraction measurement of strain and dislocation density ahead of crack tips grown in hydrogen. Acta Mater. 180, 272–286.

Creuziger, A., Bartol, L., Gall, K., Crone, W., 2008. Fracture in single crystal NiTi. J. Mechan. Phys. Solids 56, 2896–2905.

Cui, Y., Wang, T., Luo, S., Li, Z., Li, Z., 2022. A discrete–continuous model of three-dimensional dislocation elastodynamics. Int. J. Plast. 152, 103221.

Dai, Y.H., Yuan, Y., 2001. An efficient hybrid conjugate gradient method for unconstrained optimization. Ann. Oper. Res. 103, 33–47.

De Meo, D., Diyaroglu, C., Zhu, N., Oterkus, E., Siddiq, M.A., 2016. Modelling of stress-corrosion cracking by using peridynamics. Int. J. Hydrogen Energy 41, 6593–6609.

Deutges, M., Barth, H.P., Chen, Y., Borchers, C., Kirchheim, R., 2015. Hydrogen diffusivities as a measure of relative dislocation densities in palladium and increase of the density by plastic deformation in the presence of dissolved hydrogen. Acta Mater. 82, 266–274.

Devincre, B., Madec, R., Monnet, G., Queyreau, S., Gatti, R., Kubin, L., 2011. Modeling crystal plasticity with dislocation dynamics simulations: the ‘microMegas’ code. Mechan. Nano-objects 81–100.

Dong, W., Liu, H., Du, J., Huang, M., Li, Z., Chen, Z., Bobaru, F., A new peridynamic framework for discrete dislocation dynamics in 2D crystal plasticity: part II. applications. To be submitted.

Du, C., Gao, Y., Hua, Z.-.M., Zha, M., Wang, C., Wang, H.-.Y., 2022. Enhanced superplasticity achieved by disclination-dislocation reactions in a fine-grained low-alloyed magnesium system. Int. J. Plast. 154, 103300.

Dundurs, J., Mura, T., 1964. Interaction between an edge dislocation and a circular inclusion. J. Mechan. Phys. Solids 12, 177–189.

El-Awady, J.A., Biner, S.B., Ghoniem, N.M., 2008. A self-consistent boundary element, parametric dislocation dynamics formulation of plastic flow in finite volumes. J. Mechan. Phys. Solids 56, 2019–2035.

Farkas, D., Duranduru, M., Curtin, W., Ribbens, C., 2001. Multiple-dislocation emission from the crack tip in the ductile fracture of Al. Philos. Mag. A 81, 1241–1255.

Fivel, M., Canova, G., 1999. Developing rigorous boundary conditions to simulations of discrete dislocation dynamics. Modell. Simul. Mater. Sci. Eng. 7, 753.

Freund, L., 1993. The mechanics of dislocations in strained-layer semiconductor materials. Adv. Appl. Mechan. 30, 1–66.

Galvanetto, U., Mudric, T., Shojaei, A., Zaccariotto, M., 2016. An effective way to couple FEM meshes and Peridynamics grids for the solution of static equilibrium problems. Mech. Res. Commun. 76, 41–47.

Guo, X., Sun, C., Wang, C., Jiang, J., Fu, M., 2021. Study of dislocation-twin boundary interaction mechanisms in plastic deformation of TWIP steel by discrete dislocation dynamics and dislocation density-based modeling. Int. J. Plast. 145, 103076.

Henke, S.F., Shanbhag, S., 2014. Mesh sensitivity in peridynamic simulations. Comput. Phys. Commun. 185, 181–193.

Huang, M., Huang, S., Liang, S., Zhu, Y., Li, Z., 2020. An efficient 2D discrete dislocation dynamics-XFEM coupling framework and its application to polycrystal plasticity. Int. J. Plast. 127, 102647.

Huang, M., Li, Z., 2015. Coupled DDD–FEM modeling on the mechanical behavior of microlayered metallic multilayer film at elevated temperature. J. Mechan. Phys. Solids 85, 74–97.

Irani, N., Remmers, J., Deshpande, V., 2017. A discrete dislocation analysis of hydrogen-assisted mode-I fracture. Mech. Mater. 105, 67–79.

Jafarzadeh, S., Chen, Z., Bobaru, F., 2018. Peridynamic modeling of repassivation in pitting corrosion of stainless steel. Corrosion 74, 393.

Jafarzadeh, S., Chen, Z., Zhao, J., Bobaru, F., 2019. Pitting, lacy covers, and pit merger in stainless steel: 3D peridynamic models. Corros. Sci. 150, 17–31.

Jafarzadeh, S., Larios, A., Bobaru, F., 2020. Efficient solutions for nonlocal diffusion problems via boundary-adapted spectral methods. J. Peridyn. Nonlocal Model. 2, 85–110.

Jafarzadeh, S., Mousavi, F., Larios, A., Bobaru, F., 2022. A general and fast convolution-based method for peridynamics: applications to elasticity and brittle fracture. Comput. Methods Appl. Mech. Eng. 392, 114666.

Jafarzadeh, S., Wang, L., Larios, A., Bobaru, F., 2021. A fast convolution-based method for peridynamic transient diffusion in arbitrary domains. Comput. Methods Appl. Mech. Eng. 375, 113633.

Jha, P.K., Lipton, R., 2019. Numerical convergence of finite difference approximations for state based peridynamic fracture models. Comput. Methods Appl. Mech. Eng. 351, 184–225.

Kalácska, S., Ast, J., Ispánovity, P.D., Michler, J., Maeder, X., 2020. 3D HR-EBSD characterization of the plastic zone around crack tips in tungsten single crystals at the micron scale. Acta Mater. 200, 211–222.

Katiyar, A., Agrawal, S., Ouchi, H., Seleson, P., Foster, J.T., Sharma, M.M., 2020. A general peridynamics model for multiphase transport of non-Newtonian compressible fluids in porous media. J. Comput. Phys. 402, 109075.

Le, Q., Bobaru, F., 2018. Surface corrections for peridynamic models in elasticity and fracture. Comput. Mech. 61, 499–518.

Li, S., Chen, Z., Tan, L., Bobaru, F., 2018. Corrosion-induced embrittlement in ZK60A Mg alloy. Mater. Sci. Eng.: A 713, 7–17.

Liang, S., Huang, M., Li, Z., 2015. Discrete dislocation modeling on interaction between type-I blunt crack and cylindrical void in single crystals. Int. J. Solids Struct. 56, 209–219.

Liang, S., Huang, M., Zhao, L., Zhu, Y., Li, Z., 2021. Effect of multiple hydrogen embrittlement mechanisms on crack propagation behavior of FCC metals: competition vs. synergy. Int. J. Plast. 143, 103023.

Liang, S., Zhu, Y., Huang, M., Li, Z., 2019. Simulation on crack propagation vs. crack-tip dislocation emission by XFEM-based DDD scheme. Int. J. Plast. 114, 87–105.

Littlewood, D.J., 2015. Roadmap For Peridynamic Software implementation. SAND Report. Sandia National Laboratories, Albuquerque, NM Livermore, CA.

Lu, S., Kan, Q., Zaiser, M., Li, Z., Kang, G., Zhang, X., 2022. Size-dependent yield stress in ultrafine-grained polycrystals: a multiscale discrete dislocation dynamics study. Int. J. Plast. 149, 103183.

Mehrmashhadi, J., Bahadori, M., Bobaru, F., 2020. On validating peridynamic models and a phase-field model for dynamic brittle fracture in glass. Eng. Fract. Mech. 240, 107355.

Mei, T., Zhao, J., Liu, Z., Peng, X., Chen, Z., Bobaru, F., 2021. The role of boundary conditions on convergence properties of peridynamic model for transient heat transfer. J. Sci. Comput. 87, 1–22.

Nam, H.-.S., Srolovitz, D.J., 2009. Effect of material properties on liquid metal embrittlement in the Al–Ga system. Acta Mater. 57, 1546–1553.
O'day, M., Curtin, W., 2005. Bimaterial interface fracture: a discrete dislocation model. J. Mechan. Phys. Solids 53, 359–382.
Oger, L., Andrieu, E., Odemer, G., Peguet, L., Blanc, C., 2020. Hydrogen - dislocation interactions in a low-copper 7xxx aluminium alloy: about the analysis of interrupted stress corrosion cracking tests. Mater. Sci. Eng. A 790, 139654.
Oswald, J., Gracie, R., Khare, R., Belytschko, T., 2009. An extended finite element method for dislocations in complex geometries: thin films and nanotubes. Comput. Methods Appl. Mech. Eng. 198, 1872–1886.
Pagani, A., Carrera, E., 2020. Coupling three-dimensional peridynamics and high-order one-dimensional finite elements based on local elasticity for the linear static analysis of solid beams and thin-walled reinforced structures. Int. J. Numer. Methods Eng. 121, 5066–5081.
Peach, M., Koehler, J., 1950. The forces exerted on dislocations and the stress fields produced by them. Phys. Rev. 80, 436.
Seleson, P., Littlewood, D.J., 2016. Convergence studies in meshfree peridynamic simulations. Comput. Math. Appl. 71, 2432–2448.
Shewchuk, J.R., 1994. An Introduction to the Conjugate Gradient Method Without the Agonizing Pain. Carnegie-Mellon University. Department of Computer Science.
Silling, S.A., 2000. Reformulation of elasticity theory for discontinuities and long-range forces. J. Mechan. Phys. Solids 48, 175–209.
Silling, S.A., Askari, E., 2005. A meshfree method based on the peridynamic model of solid mechanics. Comput. Struct. 83, 1526–1535.
Silling, S.A., Bobaru, F., 2005. Peridynamic modeling of membranes and fibers. Int. J. Non Linear Mech. 40, 395–409.
Silling, S.A., Epton, M., Weckner, O., Xu, J., Askari, E., 2007. Peridynamic States and Constitutive Modeling. J. Elast 88, 151–184.
Sumigawa, T., Byungwoon, K., Mizuno, Y., Morimura, T., Kitamura, T., 2018. In situ observation on formation process of nanoscale cracking during tension-compression fatigue of single crystal copper micron-scale specimen. Acta Mater. 153, 270–278.
Takahashi, A., Ghoniem, N.M., 2008. A computational method for dislocation–precipitate interaction. J. Mechan. Phys. Solids 56, 1534–1553.
Tian, X., Du, Q., 2014. Asymptotically compatible schemes and applications to robust discretization of nonlocal models. SIAM J. Numer. Anal. 52, 1641–1665.
Van der Giessen, E., Deshpande, V., Cleveringa, H., Needleman, A., 2001. Discrete dislocation plasticity and crack tip fields in single crystals. J. Mechan. Phys. Solids 49, 2133–2153.
Van der Giessen, E., Needleman, A., 1995. Discrete dislocation plasticity: a simple planar model. Modell. Simul. Mater. Sci. Eng. 3, 689.
Wang, Y.U., Jin, Y., Cuitino, A., Khachaturyan, A., 2001. Nanoscale phase field microelasticity theory of dislocations: model and 3D simulations. Acta Mater. 49, 1847–1857.
Wu, P., Yang, F., Chen, Z., Bobaru, F., 2021. Stochastically homogenized peridynamic model for dynamic fracture analysis of concrete. Eng. Fract. Mech. 253, 107863.
Xu, Z., Zhang, G., Chen, Z., Bobaru, F., 2018. Elastic vortices and thermally-driven cracks in brittle materials with peridynamics. Int. J. Fract. 209, 203–222.
Zhang, G., Bobaru, F., 2016. Modeling the evolution of fatigue failure with peridynamics. The Romanian J. Technical Sci. Appl. Mechan. 61, 22–40.
Zhao, J., Jafarzadeh, S., Chen, Z., Bobaru, F., 2020. An algorithm for imposing local boundary conditions in peridynamic models on arbitrary domains.
Zhao, K., He, J., Mayer, A., Zhang, Z., 2018. Effect of hydrogen on the collective behavior of dislocations in the case of nanoindentation. Acta Mater. 148, 18–27.
Zhao, T., Shen, Y., 2021. A nonlocal model for dislocations with embedded discontinuity peridynamics. Int. J. Mech. Sci. 197, 106301.